



HAL
open science

Explosive volcanism of Piton des Neiges (Reunion Island) and excess age dispersion in sanidine: Insights into magma chamber processes in a hotspot setting

Maria Paula Castellanos Melendez, Andrea Di Muro, Oscar Laurent, Klaudia Kuiper, Jan Wijbrans, Olivier Bachmann

► **To cite this version:**

Maria Paula Castellanos Melendez, Andrea Di Muro, Oscar Laurent, Klaudia Kuiper, Jan Wijbrans, et al.. Explosive volcanism of Piton des Neiges (Reunion Island) and excess age dispersion in sanidine: Insights into magma chamber processes in a hotspot setting. *Chemical Geology*, 2023, 632, pp.121539. 10.1016/j.chemgeo.2023.121539 . hal-04246732

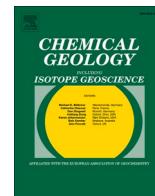
HAL Id: hal-04246732

<https://hal.science/hal-04246732>

Submitted on 17 Oct 2023

HAL is a multi-disciplinary open access archive for the deposit and dissemination of scientific research documents, whether they are published or not. The documents may come from teaching and research institutions in France or abroad, or from public or private research centers.

L'archive ouverte pluridisciplinaire **HAL**, est destinée au dépôt et à la diffusion de documents scientifiques de niveau recherche, publiés ou non, émanant des établissements d'enseignement et de recherche français ou étrangers, des laboratoires publics ou privés.



Explosive volcanism of Piton des Neiges (Reunion Island) and excess age dispersion in sanidine: Insights into magma chamber processes in a hotspot setting

Maria Paula Castellanos Melendez^{a,*}, Andrea Di Muro^{b,c,1}, Oscar Laurent^{a,d}, Klaudia Kuiper^e, Jan R. Wijbrans^e, Olivier Bachmann^a

^a Department of Earth Sciences, ETH, Zurich, Clausiusstrasse 25, CH-8092 Zürich, Switzerland

^b Université de Paris, Institut de Physique du Globe de Paris, CNRS, F-75005 Paris, France

^c Observatoire Volcanologique du Piton de la Fournaise, Institut de Physique du Globe de Paris, F-97418 La Plaine des Cafres, France

^d CNRS, Géosciences Environnement Toulouse, Observatoire Midi-Pyrénées, F-31400 Toulouse, France

^e Faculty of Science, Department of Earth Sciences, VU University Amsterdam, De Boelelaan 1085, 1081HV Amsterdam, the Netherlands

ARTICLE INFO

Editor: Balz Kamber

Keywords:

Ar-Ar dating
Piton des Neiges
Hotspot volcanoes
U-Th disequilibrium dating
Age dispersion
Explosive volcanism

ABSTRACT

Explosive eruptions of trachytic to trachyandesitic composition produced thick and widespread pyroclastic deposits during the recent volcanic activity of Piton des Neiges (PdN), the largest volcano of La Réunion Island (France). However, without precise geochronology for these eruptions, the future behavior of the dormant volcano is difficult to assess. New high-resolution single crystal $^{40}\text{Ar}/^{39}\text{Ar}$ dates on alkali feldspar, together with petrochemical data on juvenile clasts, indicate that instead of multiple and small eruptions, PdN produced a single large-volume event (“Dalle Soudée” eruption) at 198.8 ± 2.5 kyrs in which its entire crustal plumbing system was reactivated by mafic injections in the silicic reservoir. After 60 kyrs of quiescence, PdN activity resumed with several small silicic eruptions. From a dome-forming trachytic event (Belouve eruption) represented by some of the most recent block-and-ash flow deposits near the present-day summit we report in-situ $^{238}\text{U}/^{230}\text{Th}$ disequilibrium dates on pristine zircons. Sanidine and zircon crystallized at ca. 875 °C in the trachytic magma. For this event, the corresponding $^{238}\text{U}/^{230}\text{Th}$ isochron age of the zircons overlaps with the youngest $^{40}\text{Ar}/^{39}\text{Ar}$ dates on single sanidine crystals and yields an age of 42.7 ± 3.8 kyr. The variability in trace elements of zircon argues for a prolonged crystallization during this phase prior to eruption. Similarly, the $^{40}\text{Ar}/^{39}\text{Ar}$ sanidine dates show a significant spread in both eruptions, covering ca. 80 kyrs, uncommon for a method with a predicted low closure temperature. Such a pattern of age distribution argues for the presence of inherited argon in sanidines and for long residence times in the magma reservoir. The recent eruptive history of Piton des Neiges, involving evolved magma compositions, long-living silicic reservoirs and millennia-long quiescence in volcanic activity, suggests that future potentially hazardous eruptions from this volcano cannot be excluded.

1. Introduction

Silicic magmatism (rhyolite-trachyte-phonolite and the corresponding intrusive rocks) represents only a minor fraction of the total magma budget associated with intraplate basaltic volcanoes (Thordarson and Larsen, 2007; Basu et al., 2020). However, the occurrence of rare and potentially explosive, silicic magmas in intraplate settings, which typically produce frequent and dominantly effusive eruptions of low-

viscosity mafic magmas, represents a matter of serious concern in terms of volcanic hazard (Giordano et al., 2009; Preece et al., 2021). Moreover, this silicic volcanism can be associated with long quiescence times, thought to be >10 kyr for some systems (e.g., Lukács et al., 2021, Ciomadul volcano; Martí et al., 1994, Tenerife; Plesner et al., 2003, Cape Verde) and the duration of the repose times tends to correlate with eruptive volumes (Spera and Crisp, 1981).

The specific repose time of low-density, viscous silicic systems is a

* Corresponding author.

E-mail address: maria.castellanos@erdw.ethz.ch (M.P. Castellanos Melendez).

¹ Now at CNRS, Université Lyon 1, Observatoire de Lyon, Laboratoire LGL-TPE, 69622 Villeurbanne, France.

complex function of internal (volatile saturation degree) and external (recharge event, tectonic stresses, etc.) forcings, the depth and geometry of their storage, and the time scales needed to generate a given magma volume by differentiation or other magmatic processes. Available data on volcanoes around the world have shown both explosive (Connor et al., 2006; Laumonier et al., 2019; Molnár et al., 2019) and effusive (Popa et al., 2020) silicic activity after millennia-long phases of quiescence. However, the eruptive style of silicic magmas in intraplate settings remains extremely difficult to predict because of the rarity of these hazardous events. Hence, it is fundamental to assess the timescales of silicic magma accumulation and eruption in intraplate volcanoes, whose long quiescence between eruptions may lead to the perception that volcanic activity is extinct.

In this paper, we focus on the trachyte to trachyandesite eruptions of Piton des Neiges (PdN), the dormant volcano forming the largest sub-aerial part of the La Réunion intraplate volcano in the Indian ocean. La Réunion Island corresponds to the subaerial tip (ca. 3% of the whole edifice) of a 200 km large intraplate basaltic volcano (de Voogd et al., 1999; Lénat, 2016). PdN silicic eruptions represent therefore a very small fraction of the whole La Réunion magmatic budget, but a major source of hazard for the densely populated island (ca. 830.000 inhabitants). Since the birth 0.5 Myrs ago of the frequently active Piton de la Fournaise (PdF) basaltic volcano on its SE slopes (Gillot et al., 1994), PdN experienced a transition from an initial shield building stage fed by effusive basaltic activity, to a post-shield alkalic stage producing highly explosive, voluminous trachytic eruptions (Deniel et al., 1992; Salvany et al., 2012).

However, the ages of PdN explosive events and the pre-eruptive conditions of the associated magmas are still poorly known, and its recent eruptive history needs to be better constrained. We focus on the most recent explosive deposits of Piton des Neiges, in particular on i) the magmas produced by the largest explosive events of the older PN3 volcanic stage, whose composition and mineral assemblage cover the largest ranges and ii) on a recent and smaller dome-forming event of the younger PN4 stage, associated with most evolved magma compositions. Our new geochronological and petrochemical results contribute to refining the conceptual models of silicic intraplate volcanism and can help better planning for volcanic hazard mitigation in this context.

2. Geologic background

La Réunion is a huge (200 km wide, 7 km high) intraplate volcano located in the western Indian Ocean, ca. 700 km east of Madagascar (Lénat, 2016). The volcano is the youngest expression of the hotspot track that started with the production of the Deccan Traps at the K-T boundary and formed the chain of age-decreasing volcanoes of Laccadives, Maldives, Chagos, Mascarene plateau and Mauritius (Morgan, 1981; Duncan et al., 1989; Mahoney et al., 2002). Radio-isotope dating of subaerial and submarine lavas of La Réunion, suggest that volcanic activity started ca. 5 Ma ago (Upton, 1982; Gillot et al., 1994) and the subaerial activity (<2.2 Ma) progressed through the successive edification of three volcanoes: i) Piton des Neiges from >2.2 to 0.027–0.012 Ma (McDougall, 1971; Delibrias et al., 1986; Deniel et al., 1992; Quidelleur et al., 2010; Salvany et al., 2012; Famin et al., 2022) being the largest and oldest, ii) the Alizés volcano, built on the SE slope of Piton des Neiges and now largely dismantled and buried by the lavas of the youngest iii) Piton de la Fournaise shield volcano whose activity started ca. 0.53 Ma ago (Gillot and Nativel, 1989; Gillot et al., 1994). Piton de la Fournaise volcano is very active with several eruptions per year on average and is currently in its shield building stage (Roult et al., 2012; Albarède et al., 1997).

Piton des Neiges (3.1 km a.s.l) is currently in its post-shield phase, since the building of Piton de la Fournaise shield volcano on its SE slopes (Gillot et al., 1994). It shows a deeply dissected morphology, due to extensive erosion in a wet tropical environment, exposing a set of intrusive bodies (gabbro; wherlite; dunite; syenite) related to the

different phases of activity of the volcano (Berthod et al., 2020). PdN is the site of frequent and deep seismic activity (Duputel et al., 2021) and hosts permanent hydrothermal systems (Rançon and Rocher, 1985; Marty et al., 1993; Sanjuan et al., 2000; Bénard et al., 2020; Boudoire et al., 2020). Previous studies have shown that the compositions of Piton des Neiges magmas have evolved in time from olivine-rich basalts emitted during the early shield phase to more alkaline and silicic magmas (plagioclase-rich basalts, hawaiite, mugearites, benmoreites, trachytes and comendites) in the post-shield stage (Upton and Wadsworth, 1966, 1967; McDougall, 1971; Nativel, 1978; Gillot and Nativel, 1982; Fisk et al., 1988; Gillot et al., 1994; Kluska, 1997; Quidelleur et al., 2010; Smietana, 2011; Salvany et al., 2012; Gayer et al., 2019).

Available data suggest that the activity of Piton des Neiges has fluctuated considerably over time, with the building of three successive basaltic shield volcanoes (> 1.8 Ma: the so-called “La Montagne” edifice; 1.4–0.95 Ma: PN1 stage; 0.65–0.43 Ma: PN2 stage) followed by two young stratocones (0.34–0.18 Ma: PN3 stage and 0.14–0.027 Ma: PN4 stage), all interrupted by long-lasting repose periods (McDougall, 1971; McDougall and Watkins, 1973; Gillot and Nativel, 1982; Baksi et al., 1993; Gillot et al., 1994; Raïs et al., 1996; Kluska, 1997; Baksi and Hoffman, 2000; Quidelleur et al., 2010; Singer et al., 2014; Famin et al., 2022). The base of the PN3 stage is represented by feldspar-rich alkaline porphyritic lavas, locally called “Pintades” (Albarède et al., 1997; Valer et al., 2017). According to available geochronology, PN3 and PN4 stages are separated by a ~ 40 kyrs quiescence phase and both stages seem to be dominated by silicic explosive activity near the end of their cycles (Salvany et al., 2012; Kluska, 1997). However, considerable uncertainty remains on the youngest known silicic eruption of Piton des Neiges, for which published ages span ca. 24 ka depending on the dating technique used, i.e. 36.5 ± 2.3 ka for U-Th-disequilibrium dating combined with (U-Th)/He dating of zircon (Famin et al., 2022); 29.5 ± 3.0 ka and 29.0 ± 4.0 ka for K/Ar dating of lava groundmass (Gillot and Nativel, 1982; Kluska, 1997); 21.9 ± 0.7 ka for ^{14}C dating of charcoal (Delibrias et al., 1986) and 12.5 ± 3.0 ka for $^{238}\text{U}/^{230}\text{Th}$ dating of whole rock (Deniel et al., 1992). Nevertheless, Famin et al. (2022) suggest in their recent review of ^{14}C ages that the last eruption of PdN should be placed at ca 27 ka. Hence, this study focuses on the explosive eruptive products of the two stages of stratocone building documented in the post-shield phase (PN3 and 4), in an attempt to better constrain the last phases of activity of the volcano and foresee its behavior in the future.

3. Materials: outcrop and sample descriptions

Several thick ignimbrite packages, ranging from loose to densely welded, are found on the western and southern flanks of Piton des Neiges (Fig. 1). These deposits are associated with the oldest post-shield stage of Piton des Neiges (PN3). Samples from different levels of the erupted sequence were collected during a field campaign in May 2018 from the areas of Saint Pierre (24–3, 24–4, 26–1, 28–1 and 28–2), Saint Louis (28–3), Saint Gilles (23–5) and Maïdo (23–1, 23–3 and 23–4). A complete list of the samples and their stratigraphic position in each location is presented in the Supplementary Data: Appendix B.

The stratigraphic sequence can be generalized for all localities, except at Maïdo. Basaltic lava flows are overlain by a more silicic pyroclastic sequence, lava flows and tephra being separated by a red paleo-soil. The base of the pyroclastic sequence is formed by cm-thick ash layers. The basal ash is covered by a pumice-rich fall out deposit, several tens of cm-thick, followed by a several meter-thick (up to 15 m) ignimbrite package (Fig. 1). The thickness of the different pyroclastic deposits, especially of the ignimbrite, varies significantly. At Maïdo only the ignimbrite is observed, ranging from welded to loose. Many loose or sintered pyroclastic deposits cropping out in the Saint Pierre area seem to contain a high proportion of groundmass glass and remain unaltered. Macroscopic evidence of magma mingling is abundant in these deposits as banded juvenile blocks. The fall out and ignimbrite deposits from all localities contain petrographically similar trachyandesitic pumices that

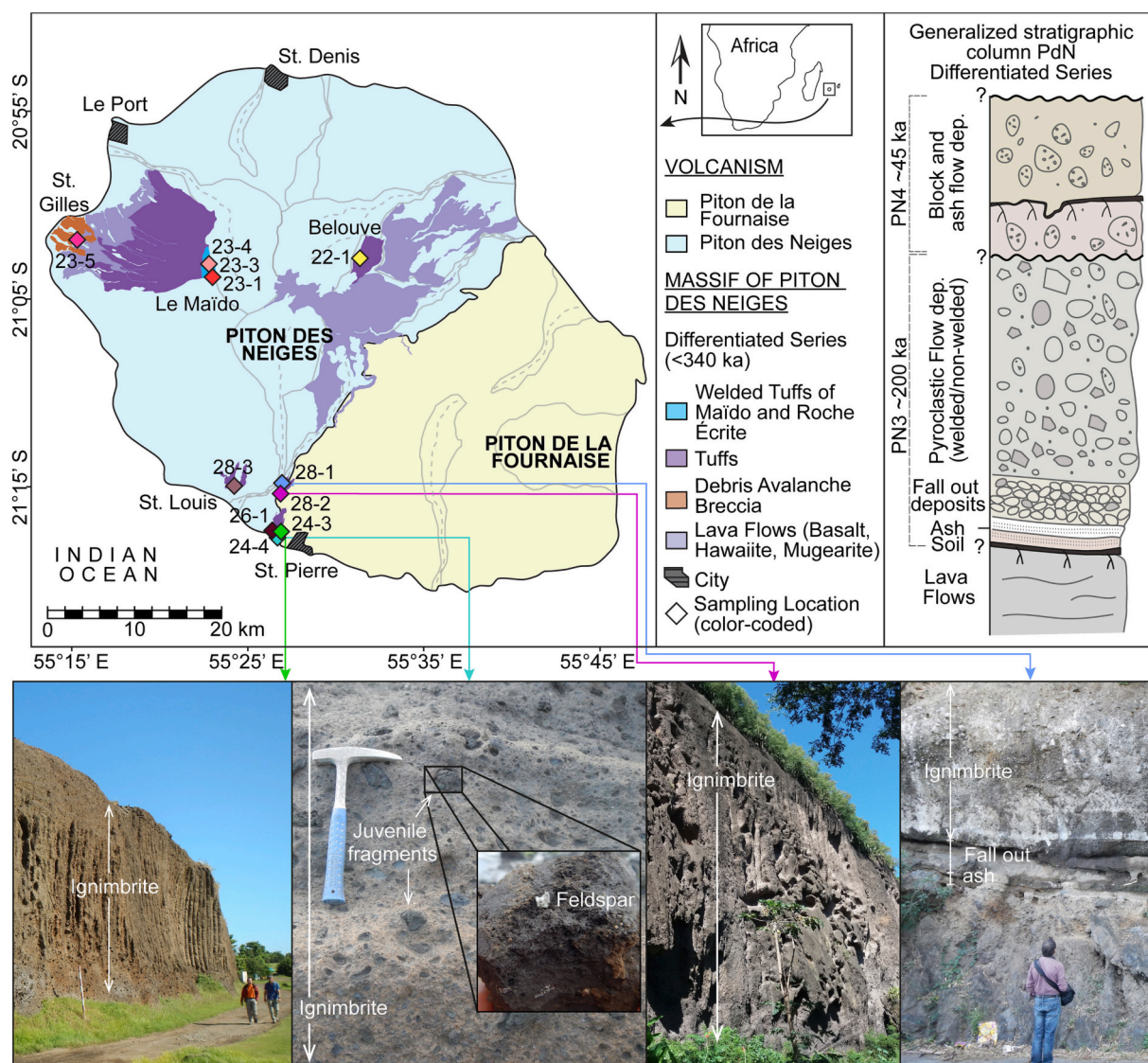


Fig. 1. Top, A: Simplified geological map of La Reunion Island (modified from BRGM (Cartographe), 2006) with color coded sample locations. B: Generalized stratigraphic column for the eruptive sequences of PN3 and PN4 stages of PdN studied here. Bottom: Field photographs of sample locations showing thick ignimbrite packages (28–2 and 24–3) hosting crystal poor juvenile fragments with several mm-long feldspar phenocrysts (24–4) and overlying fall out and ash layers (28–1).

were collected for this study. The pumice clasts contain olivine, plagioclase, alkali feldspar, pyroxene, amphibole and oxide phenocrysts in variable amounts.

As part of the younger post-shield stage (PN4), smaller volume explosive eruptions were emplaced as a set of pumiceous pyroclastic flows and block-and-ash flow deposits found in the Belouve area (Fig. 1). In these deposits, attributed to a set of discrete explosive episodes and lava dome collapses, juvenile blocks look homogeneous and lack macroscopic evidence of magma mingling. Sample 22–1 from Belouve differs from all others from PN3. It is crystal-rich (~30%) and contains phenocrysts of only fayalitic olivine, plagioclase, alkali feldspar, pyroxene, amphibole, Fe-oxides and biotite. The groundmass is microcrystalline with mainly alkali feldspar and minor amounts of quartz. Zircon is also present, which makes the sample one of the few described occurrences of this accessory phase in volcanic deposits of La Reunion Island.

4. Methods

Unweathered and unaltered, individual pumice clasts from the fallout or from the ignimbrite levels of the pyroclastic sequence from all

localities were analyzed for major and trace elements. Gem-quality sanidine crystals from representative samples were separated for high-precision $^{40}\text{Ar}/^{39}\text{Ar}$ analysis on single crystals using a multi-collector Thermo Fisher Scientific Argus VI+ mass spectrometer at the Argon Geochronology Laboratory, Vrije Universiteit Amsterdam. Given the dispersion in $^{40}\text{Ar}/^{39}\text{Ar}$ sanidine dates calculating a global weighted mean age was not considered suitable. Instead, a Bayesian statistical model for complex age distributions was used to calculate an eruption age (Keller et al., 2018; Van Zalinge et al., 2022); using a modified version of the code available at: <https://github.com/brenhinkeller/BayeZirChron.c>. The modification of the code includes an exponential distribution of the relative age of crystallization or apparent closure before eruption (Van Zalinge et al., 2022). In addition, three weighted mean ages were calculated for each sample applying different data filtering methods following Schaen et al. (2021): 1) low MSWD weighted mean filter, 2) weighted mean filter, and 3) normality test and MSWD filter.

Zircon grains from the block-and-ash flow from Belouve (22–1) were separated from the crushed sample, hand-picked and set in Epoxy mounts. Some grains were polished to a sub-equatorial section, whereas others were left unpolished to analyze the outermost rims. Zircon

$^{238}\text{U}/^{230}\text{Th}$ dating and trace element analysis was performed by laser ablation – inductively coupled plasma – mass spectrometry (LA-ICP-MS) at the Institute of Geochemistry and Petrology, ETH Zürich, using an ASI RESOLUTION excimer ArF (193 nm) laser ablation system coupled to a Thermo Fisher Element XR sector field ICP-MS and following the method described by [Guillong et al. \(2016\)](#).

Additionally, feldspar and olivine, as the most abundant phases in all samples, were also separated from crushed samples and analyzed for major elements by electron microprobe (EPMA). Groundmass and exposed glassy olivine-hosted melt inclusions were analyzed for major elements using an EDS-SEM. Trace elements of olivine-hosted melt inclusions were also obtained by LA-ICP-MS. All geochemical analyses were carried out at the Institute of Geochemistry and Petrology, ETH Zürich. Average melt inclusion compositions were used to model the thermochemical evolution of the melt with 2 and 4 wt% H_2O at 2 kbar using the software Rhyolite-MELTS v1.2.x ([Gualda et al., 2012](#); [Ghiorso and Gualda, 2015](#)). Zircon saturation temperatures ([Boehnke et al., 2013](#)) and the TiO_2 solubility ([Hayden and Watson, 2007](#)) and activity (a_{TiO_2}) of the melt were calculated for the modeled composition. The activity of Ti at zircon saturation was then used to obtain Ti-in-zircon temperatures ([Loucks et al., 2020](#); [Ferry and Watson, 2007](#)). Alkali-feldspar-melt thermometry was performed only for the Belouve sample following [Putirka \(2008\)](#) with equilibrium tests from [Mollo et al. \(2015\)](#). A detailed methodology description is provided in the Supplementary Data: Appendix A.

5. Results

5.1. Geochemistry

The composition of bulk lavas that are discordantly overlain by the pyroclastic deposits in Saint Pierre (locations 28–1 and 26–1) is basaltic to trachybasaltic (ca. 45 wt% SiO_2 ; 4–5 wt% $\text{Na}_2\text{O} + \text{K}_2\text{O}$), while the bulk pumices from the PN3 explosive deposits (Saint Pierre, Saint Gilles, Saint Louis and Maïdo) range from basaltic-trachyandesitic to

trachyandesitic, with a concomitant increase in SiO_2 (from ca. 52 to ca. 60 wt% respectively) and alkalis ($\text{Na}_2\text{O} + \text{K}_2\text{O}$ from ca. 7 up to ca. 9 wt% respectively; [Fig. 2](#), Appendix B). The groundmass glass from the same pumice samples shows more evolved, trachyandesitic to trachytic-trachydacitic compositions (58–63 wt% SiO_2 ; 9–11 wt% $\text{Na}_2\text{O} + \text{K}_2\text{O}$; [Fig. 2](#)) and contains microlites mainly of feldspar and Fe-Ti oxides with interstitial glass. Melt inclusions hosted in fayalitic olivine from the Belouve deposit (PN4) are glassy with a bubble and of trachytic-trachydacitic to rhyolitic composition (65–70 wt% SiO_2 ; 11–12 wt% $\text{Na}_2\text{O} + \text{K}_2\text{O}$; [Fig. 2](#)), and their average Zr and Ti concentrations are 644 and 1213 ppm, respectively. Altogether, the compositional variation of the eruptive products of PN3 (lavas, bulk pumices and groundmass) to the melt inclusions in PN4 Fe-rich olivine is consistent with an alkaline differentiation trend.

In Saint Pierre, Saint Louis, Saint Gilles and Maïdo, plagioclase, alkali feldspar and olivine coexist and show a wide range of compositions. Plagioclase varies from bytownite (An_{88}) to oligoclase (An_{23}) with the main population concentrated around An_{40-50} and alkali feldspar from anorthoclase (Or_{18}) to sanidine (Or_{44} ; [Fig. 2](#)). Texturally, plagioclase or alkali feldspar occur as euhedral, subhedral or anhedral crystals, which are generally unzoned ([Fig. 3](#)). When present, zonation is normal or reverse. Normal zonation in plagioclase is indicated by a decrease in An from core to rim with generally along a small compositional gradient (e.g., An_{85} to An_{83} , An_{48} to An_{46}). In rare occasions An-rich plagioclase exhibits zonation from An_{87} to An_{58} from core to rim. Reverse zonation occurs as a small increase in An content from rim to core (e.g., An_{45} to An_{48} , An_{23} to An_{26}). In alkali feldspar, chemical zonation can be present as increase in orthoclase component towards the rim (e.g., Or_{31} to Or_{38} , Or_{33} to Or_{35} , Or_{27} to Or_{32}). Olivine compositions range from forsterite- or fayalite-rich in the same sample, varying from Fo_{03} to Fo_{88} , with main populations falling between Fo_{37} and Fo_{45} ([Fig. 2](#); Appendix B). Along the entire compositional range, olivine can be found as euhedral, but also present anhedral crystals with resorption embayment. Zonation in olivine is rare, with only a few grains showing micrometer-thin rims with sharp compositional changes converging towards a similar

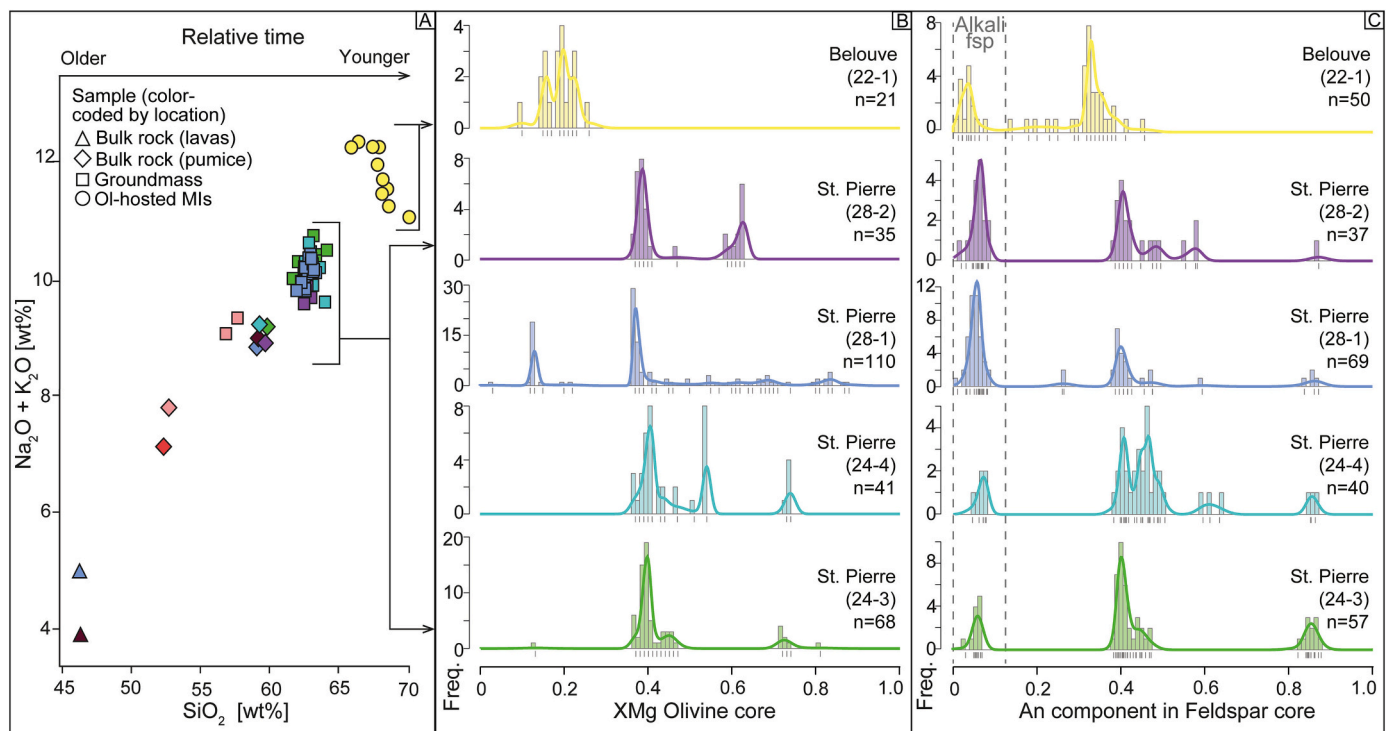


Fig. 2. A: Silica vs total alkalis diagram of all analyzed samples for bulk rock, groundmass glass and averaged olivine-hosted melt inclusions. Only glassy melt inclusions (MIs) hosted in fayalitic olivine were analyzed. B, C: XMg in olivine cores and An content in feldspar cores, respectively, for representative samples from Saint Pierre and Belouve.

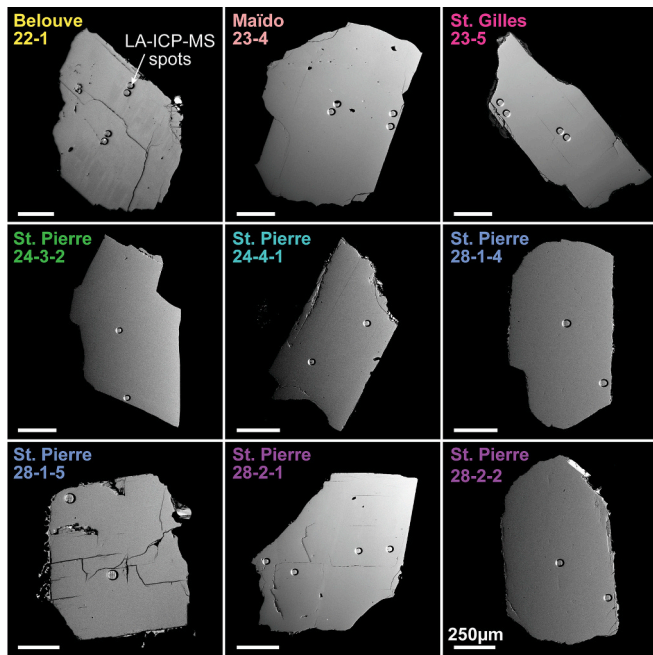


Fig. 3. Backscattered electron images of alkali feldspar in all studied samples (color-coded). Alkali feldspar is generally euhedral to subhedral and unzoned. In Belouve, exsolution textures are observed within a narrow compositional range (e.g., Or₃₁ to Or₄₃). Scale bar in white in all images is equal to 250 µm. Visible spots on the alkali feldspar are LA-ICP-MS spot analyses.

composition around Fo_{55–65}. Equilibrium tests (following Putirka, 2008) indicate disequilibrium between the groundmass glass and the crystal cargo for both feldspar and olivine. Only intermediate mineral compositions could have been crystallized from a melt having the composition of the accompanying groundmass in PN3 samples from Saint Pierre, Saint Louis, Saint Gilles and Maïdo.

In the PN4 Belouve block-and-ash flow, feldspar and olivine compositions span narrower ranges than in the PN3 Saint Pierre, Saint Louis, Saint Gilles and Maïdo samples. Plagioclase varies from andesine (An₄₆) to oligoclase (An₁₄) and presents well-developed normal zonation (decreasing An content) from core to rim. It occurs as euhedral to subhedral grains and commonly exhibit corroded cores. Alkali feldspar crystals from anorthoclase (Or₁₄) to sanidine (Or₄₅) are subhedral to anhedral and some show thin exsolution lamellae with slight variations in orthoclase content (e.g., from Or₃₁ to Or₄₃; Fig. 3). Alkali feldspar is generally unzoned and when zonation is present it could be either normal or reverse, depending on the increase or decrease of orthoclase component from core to rim, respectively. However, observed zonation spans narrow compositional variations (e.g., Or₂₈ to Or₃₁ or Or₂₈ to Or₂₅ from core to rim). Olivine occurs as anhedral and partially resorbed grains of compositions that range from Fo₀₉ to Fo₂₆ (Fig. 2) and that sometimes show narrow inverse zonation. Crystallization temperatures for the alkali-feldspar were only possible to calculate for the Belouve sample, using the olivine-hosted-MIs as the equilibrium melt (corrected for post-entrapment crystallization). These temperatures spread over a narrow range from 830 °C to 875 °C, in agreement with the modeled phase proportions obtained with Rhyolite-MELTS for a melt with 4 wt% H₂O (Fig. 4). Alkali-feldspar crystallization temperatures for other samples could not be calculated because an equilibrium melt composition could not be found.

Zircon was found only in the block-and-ash-flow from Belouve (PN4; sample 22-1). The saturation temperature for zircon (T_{zrc-sat}) in this sample was calculated following the Boehnke et al. (2013) calibration and the Rhyolite-MELTS model at 4% H₂O resulting in a temperature of ~875 °C. At these conditions, the Ti activity (aTiO₂) of the system is 0.32, which we used for Ti-in-zircon thermometry (Fig. 4C; see

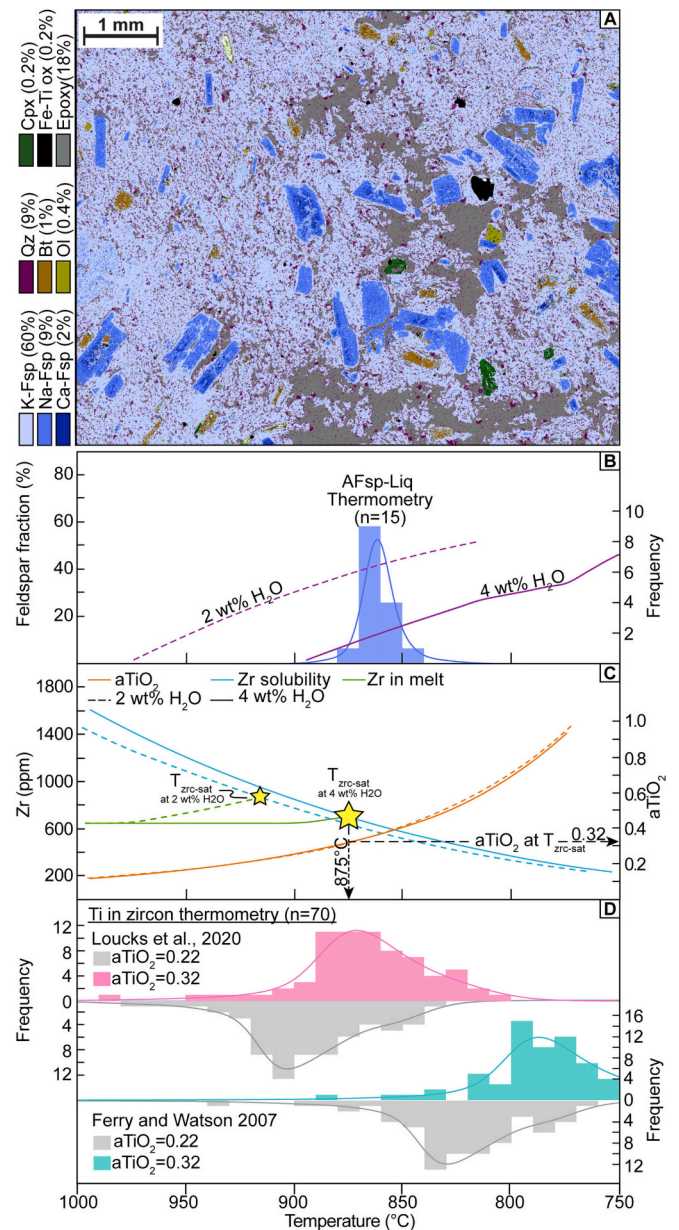


Fig. 4. A: Phase map of a polished thin section from sample 22-1 measured by EDS-SEM obtained using the software iSpectra (Liebske, 2015) to calculate mineral phase proportions. B: Alkali feldspar-melt thermometry following Putirka (2008), and evolution of the feldspar fraction for a fractionating melt composition with initial 2 wt% H₂O (dashed line) and 4 wt% H₂O (solid line). C-D: Zr solubility, Zr content and Ti activity in the melt with decreasing temperature. Stars indicate the moment of zircon saturation when Zr solubility and Zr content curves intersect for a melt with initially 2 wt% H₂O (dashed lines) or 4 wt% H₂O (solid lines). The temperature of zircon saturation (T_{zrc-sat}) is derived projecting that intersection with the temperature axis. Likewise, the intersection with the Ti activity curve defines the Ti activity in the melt at the moment of zircon saturation, used to calculate Ti-in-zircon temperatures (D) following Loucks et al. (2020) and Ferry and Watson (2007).

Supplementary Data: Appendix A). Ti contents in core, rim and outermost rim vary between ~3 and 9 ppm and resulting temperatures follow a normal distribution around a mean of 868 °C using the calibration of Loucks et al. (2020), and around 784 °C following Ferry and Watson (2007); (Fig. 4D). The first calibration provides crystallization temperatures that agree with the estimated T_{zrc-sat} and with most of the estimated alkali-feldspar-melt temperatures. Calculations were also made for aTiO₂ of 0.22, obtained using the Rhyolite-MELTS model at

2% H₂O, to assess the impact of aTiO₂ on obtained temperatures. The decreased aTiO₂ results in an average increase between 30 and 40 °C in zircon crystallization temperatures.

Other trace element distributions in zircon, unlike Ti, vary systematically between core, rim and outermost rims. All analyses define a positive correlation between U/Th and Ce anomalies, used as a proxy for the oxidation state of the magma, where the lower ratios and Ce anomalies represent the outermost parts of the zircons (Fig. 6C). The Nb concentrations also decrease with decreasing Ti for core and rim analyses in polished grains, which can be used as a proxy for differentiation. Unpolished grains vary in Ti contents but contain the lowest Nb concentrations (Fig. 6D; Appendix B).

5.2. Geochronology

5.2.1. ⁴⁰Ar/³⁹Ar dating

Sanidine crystals from Saint Pierre, Saint Gilles and Maïdo of the PN3 stage show a well-defined overlap for the youngest ⁴⁰Ar/³⁹Ar dates and describe a similar trend to progressively older dates (Fig. 5A). Kernel density diagrams of single crystal ⁴⁰Ar/³⁹Ar dates in each sample illustrate bimodal to multimodal distributions where the highest peaks overlap with the youngest population of dates. The youngest and oldest grains in each sample are presented in Table 1 together with a Bayesian estimate of the eruption age (individual results for all aliquots are given in the Supplementary Data: Appendix C). These Bayesian estimates indicate an eruption age that overlaps with the youngest population of each sample and that is reproducible, within uncertainty, among all PN3 samples from Maïdo, Saint Gilles and Saint Pierre. Additionally, weighted mean ages were calculated for the youngest population with an acceptable MSWD (method 1), for the youngest population for which the difference between the weighted mean age and the next older age is greater than zero (method 2) and for the largest population of dates with acceptable MSWD that describe a normal distribution (method 3; following Schaen et al., 2021). Generally, methods 1 and 2 provide the same results for all samples, except for sample 24–3-2. These weighted mean ages are consistent with the Bayesian calculations of the eruption

age. For sample 24–3-2, an acceptable MSWD was not attainable on a weighted mean age for any set of the youngest dates. Method 3 results are equivalent to method 1 and 2 for 4 samples (23–4, 24–4-1, 28–1-5 and 28–2-2). In samples 23–5 and 24–3-2, method 3 results in weighted mean ages that are older than those calculated with methods 1 and 2 and the Bayesian estimate.

Due to the correlation of Bayesian eruption ages and weighted mean ages (methods 1 and 2) between all samples from Maïdo, Saint Gilles and Saint Pierre, all single crystal ⁴⁰Ar/³⁹Ar dates were also combined as one single population for which all corresponding ages were calculated (Table 1, Fig. 5B). A kernel density diagram of the combined data illustrates a multimodal distribution of single crystal dates where the highest peak does not overlap with the youngest population but with intermediate dates. Other modes occur with lower frequencies at younger and older ranges. The estimated Bayesian eruption age is 198.8 ± 2.5 ka and overlaps within uncertainty with the weighted mean ages 1 and 2. The third weighted mean returns an age that is slightly older.

In Belouve (PN4 stage; sample 22–1), single sanidine ⁴⁰Ar/³⁹Ar dates are younger, from 42.6 ± 2.1 ka to 73.4 ± 1.8 ka and describe a bimodal distribution with one older outlier where the highest peak overlap with the youngest dates (Fig. 5A). The Bayesian eruption age is estimated at 42.7 ± 3.8 ka, consistent with weighted mean ages 1 and 2. In this sample, method 3 results in a weighted mean age that is significantly older than the others (52.3 ± 1.4 ka). The oldest crystal in this sample yields a 219.5 ± 18.8 ka date and was not included in any age calculation due to its significantly large distance to the rest of the population (~170 kyr).

Obtained K/Ca ratios from ⁴⁰Ar/³⁹Ar analysis do not show any systematic correlation with obtained dates and are within the range of typical K/Ca ratios measured on alkali feldspars by EPMA. This indicates that the dated crystals were indeed alkali feldspars and that the dated population was representative of the population geochemically characterized by major and trace element analysis.

5.2.2. ²³⁸U/²³⁰Th disequilibrium dating

A total of 193 spots were measured for ²³⁸U/²³⁰Th disequilibrium

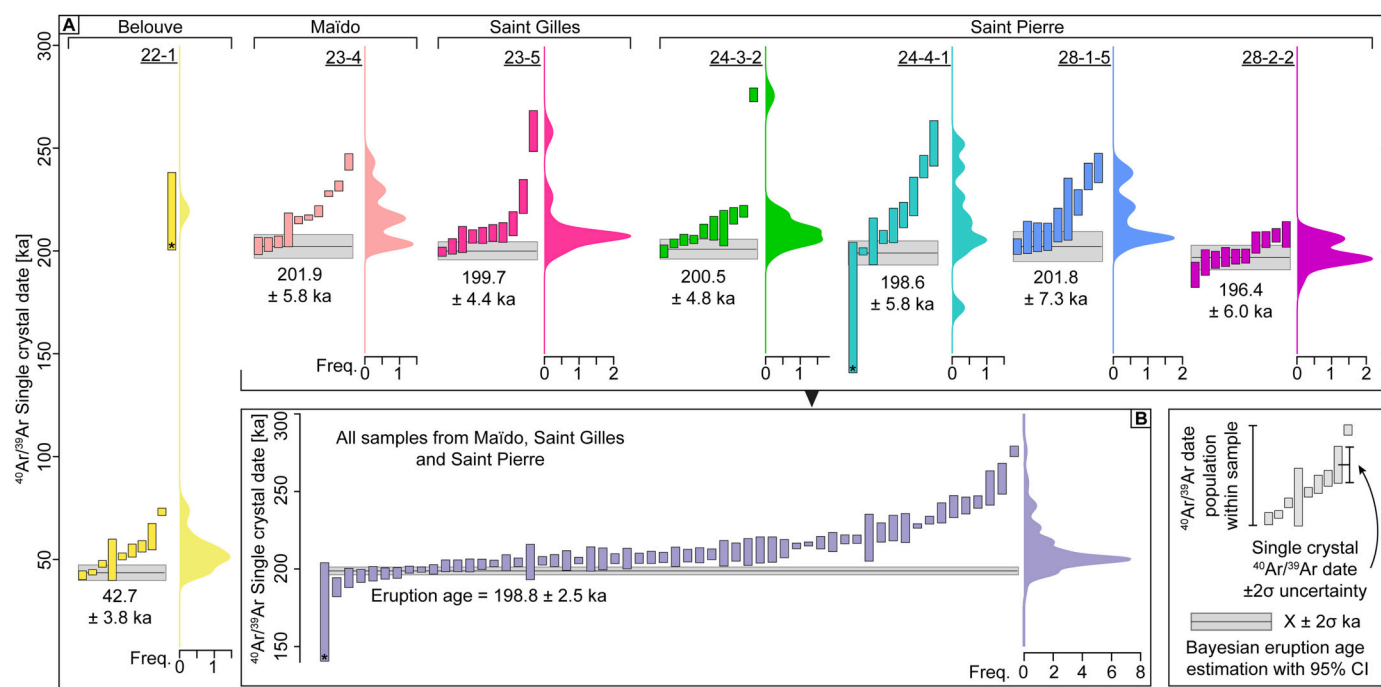


Fig. 5. A: ⁴⁰Ar/³⁹Ar dates [ka] for single alkali feldspar crystals with its 2σ uncertainty and the estimated eruption age within 95% confidence interval (CI) following a Bayesian statistical model modified after Keller et al. (2018). A kernel density diagram is shown for each sample. B: Combined single crystal dates for all samples from Maïdo, Saint Gilles and Saint Pierre with their kernel density distribution and the Bayesian estimation of the eruption age for the combined dataset.

Table 1

Summary of $^{40}\text{Ar}/^{39}\text{Ar}$ dating results. For each sample, the youngest and oldest single crystal dates are presented and the total number of dates available (n). The Bayesian estimation of the eruption age is listed for each sample. The youngest date in sample 24–4–1 and the oldest date in sample 22–1 were not included in the Bayesian calculation. Three weighted mean ages calculated with three different filtering methods following Schaen et al. (2021) are also reported for each sample with the corresponding MSWD and number of analyses included in each calculation (n). All single crystal dates from Maïdo, Saint Gilles and Saint Pierre were also combined to calculate all reported ages. All ages are given with their 2σ uncertainty.

Location/Sample	Youngest and oldest Single crystal age [ka]			Bayesian estimates of eruption age [ka]		1. Low MSWD weighted mean filter				2. Weighted mean filter				3. Normality test and MSWD filter				
	Age [ka]	$\pm 2s$	n	Age [ka]	$\pm 2s$	Age [ka]	$\pm 2s$	MSWD	n	Age [ka]	$\pm 2s$	MSWD	n	Age [ka]	$\pm 2s$	MSWD	n	
Belouve 22–1	42.6	2.1	10	42.7	3.8	43.7	1.1	1.3	2	43.7	1.1	1.3	2	52.3	1.4	1.3	3	
	73.4	1.8																Not included
	219.5	18.8																
Maïdo 23–4	202.3	4.2	10	201.9	5.8	203.8	1.9	1.1	4	203.8	1.9	1.1	4	203.8	1.9	1.1	4	
	243.2	4.0																
St. Gilles 23–5	199.5	2.2	10	199.7	4.4	200.6	1.8	2.0	3	200.6	1.8	2.0	3	207.0	1.6	2.1	7	
	258.2	9.9																
St. Pierre 24–3–2	199.8	3.0	10	200.5	4.8	Low MSWD test not achieved				204.0	1.2	3.7	4	206.5	1.4	2.1	5	
	275.9	3.4																Not included
	172.3	31.7																
St. Pierre 24–4–1	199.6	1.7	9	198.6	5.8	199.7	1.7	1.9	3	199.7	1.7	1.9	3	199.7	1.7	1.9	3	
	252.2	11.0																
	202.0	3.8																
St. Pierre 28–1–5	240.2	7.1	9	201.8	7.3	205.4	2.6	2.1	6	205.4	2.6	2.1	6	205.4	2.6	2.1	6	
	240.2	7.1																
St. Pierre 28–2–2	188.3	6.1	10	196.4	6.0	195.9	1.8	1.6	6	195.9	1.8	1.6	6	195.9	1.8	1.6	6	
	207.9	6.2																
Maïdo+ S. Gilles+ S. Pierre	172.3	31.7	58	198.8	2.5	195.8	1.8	1.7	7	199.3	0.9	2.8	14	205.8	0.7	1.5	17	
	275.9	3.4																

dating of PN4 zircons, including 59 from cores and rims of polished grains and 41 from outermost rims of unpolished grains. All results together define an isochron date of 44.8 ± 1.3 ka (2σ , MSWD = 1.2; $n = 193$) with an initial $^{230}\text{Th}/^{232}\text{Th}$ of 0.871 ± 0.033 (Fig. 6A). This age agrees with the youngest population of single sanidine $^{40}\text{Ar}/^{39}\text{Ar}$ dates from the same sample from Belouve, the estimated eruption age and the

weighted mean ages derived by methods 1 and 2, and is also very close to the less precise U/Th age (36 ± 7 ka) obtained by Deniel et al. (1992) on a block from a pyroclastic deposit sampled in the same area. No older zircons in secular equilibrium have been found, indicating that there is no evidence in the magma for recycling of continental crust under Piton des Neiges (Nauret et al., 2019) but that they all crystallized within the

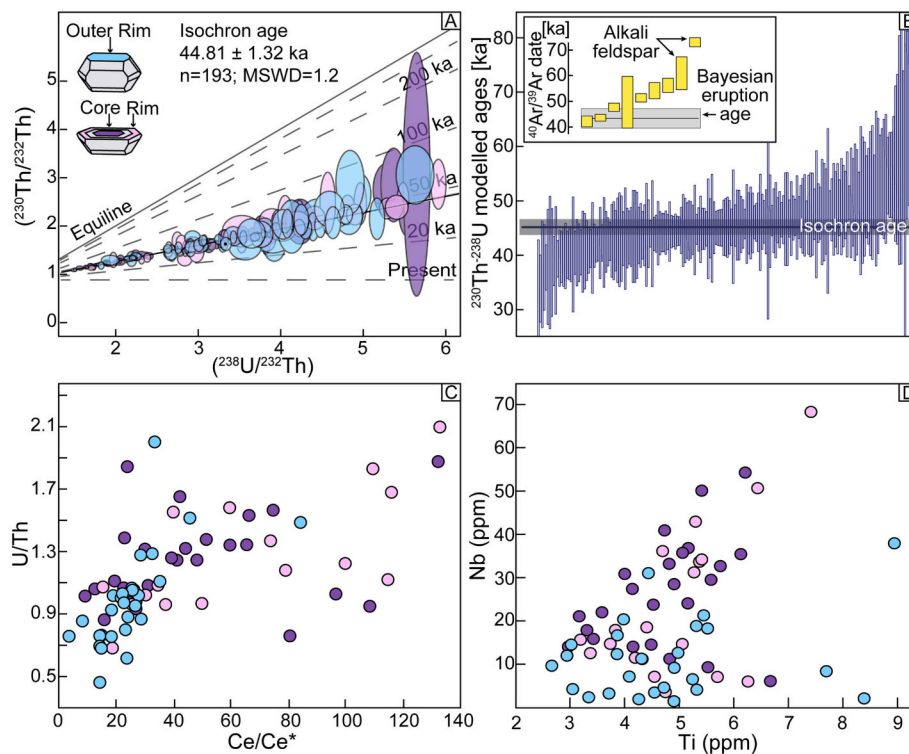


Fig. 6. A: ^{238}U - ^{230}Th isochron for 193 LA-ICPMS spot analyses on zircon grains from sample 22–1. Spot analyses were carried out on the outermost rim of unpolished grains and on rims and cores of polished grains. B: ^{230}Th - ^{238}U modeled ages (2σ) compared to $^{40}\text{Ar}/^{39}\text{Ar}$ single sanidine dates and the Bayesian estimate of the eruption age. C-D: Plots of U/Th vs. Ce/Ce* and Nb vs. Ti contents in zircon, respectively.

PdN magmatic system.

Modeled individual ^{230}Th - ^{238}U dates were obtained for each analysis using the isochron intercept to estimate the initial $^{230}\text{Th}/^{232}\text{Th}$ ratio, spanning from 33.1 ± 9.9 ka to 72.4 ± 23.8 ka (2σ ; Fig. 6B). As this range is comparable to that defined by single sanidine $^{40}\text{Ar}/^{39}\text{Ar}$ dates from the sample (42.6 ± 2.1 ka to 73.4 ± 1.8 ka), it is possible that zircon grains have crystallized over a protracted period of several tens of kyr. Nevertheless, as 94% (182 out of 193) of the individual ^{230}Th - ^{238}U dates overlap within 2σ uncertainty with the isochron date of 44.8 ± 1.3 ka obtained from the whole population, we still regard this isochron as representative of the $^{238}\text{U}/^{230}\text{Th}$ disequilibrium eruption age. This is also consistent with the Bayesian eruption age of 42.7 ± 3.8 ka obtained from sanidine $^{40}\text{Ar}/^{39}\text{Ar}$ data.

6. Discussion

6.1. Defining $^{40}\text{Ar}/^{39}\text{Ar}$ eruption ages

Recent advancements in $^{40}\text{Ar}/^{39}\text{Ar}$ dating allow us to progressively obtain single crystal dates with lower analytical uncertainty. However, due to the improved analytical precision the observed dispersion in data sets of individual dates is increasingly expanding. As a consequence, the interpretation of such dates and the definition of ages with geological significance (e.g., eruption ages) becomes more challenging (e.g., see discussion in Schaen et al., 2021). Several authors have used different approaches to define eruption ages from a disperse dataset including: 1) Progressively excluding the oldest single crystal date from a weighted mean calculation until the obtained MSWD falls below a critical value (Stelten et al., 2015); 2) Calculating a weighted mean age for the youngest population of single sanidine plateau dates for which the difference between the weighted mean of the youngest group and the next older date is greater than zero (Andersen et al., 2017); 3) Applying a ‘youngest gaussian’ filter with an acceptable MSWD and calculating a global mean from all available ages (Ellis et al., 2017); or 4) adopting the Bayesian approach of Keller et al. (2018) modified for $^{40}\text{Ar}/^{39}\text{Ar}$ dates (Van Zalinge et al., 2022). As suggested by Schaen et al. (2021) and exemplified above, we report the three different weighted mean ages for our $^{40}\text{Ar}/^{39}\text{Ar}$ dates (1–3) and the Bayesian estimations of the eruption ages for each sample (4). The integrations of these approaches allowed us to define a robust date that could be confidently interpreted as an eruption age.

Applying approaches 1 and 2 results in identical weighted mean ages in all studied samples that are indistinguishable from the respective Bayesian calculations (Table 1). Furthermore, in the majority of the samples, the weighted means obtained following approach 3 are also identical to those obtained with methods 1 and 2. These results indicate that the estimated ages are highly reproducible, regardless of the method used to calculate them, and support the robustness of the obtained ages and their geological significance. In cases where weighted means of a normally distributed population (method 3) are older than those obtained through methods 1, 2 or 4 (samples 22–1, 23–5 and 24–3–2), we suggest that these ages are not representative of the eruption age. Instead, they could be the result of the incorporation of extraneous Ar in the crystal prior eruption as discussed below.

The Bayesian calculation of the eruption age for a given dataset is the only approach that includes all available dates while considering the pre-eruptive distribution of crystallization or apparent closure ages. Additionally, this method is less likely to underestimate the uncertainties on a given age (Keller et al., 2018; Van Zalinge et al., 2022). Therefore, we favor the Bayesian estimates over any weighted mean, regardless of the filtering method used, when dealing with largely dispersed single crystal $^{40}\text{Ar}/^{39}\text{Ar}$ dates and consider those dates as the eruption ages of the pyroclastic sequences studied here.

6.2. Recent explosive activity at Piton des Neiges

High precision $^{40}\text{Ar}/^{39}\text{Ar}$ analyses on alkali feldspar, coupled to zircon U/Th ages on the most recent deposits of Piton des Neiges, allowed us to define more precisely the eruptive activity of this volcano in the last 200–300 kyrs (PN3 and PN4). In contrast to the interpretations of Kieffer et al. (1993) and Kluska (1997), who suggest two main phases occur at the end of the PN3 stage, namely the “Dalle Soudée” event (221 ± 3 ka, obtained by dating an underlying lava flow) in Maïdo and the ignimbritic phase (190–180 ka), our new data suggest that the “Dalle Soudée” event is slightly younger (201.9 ± 5.8 ka, probably reflecting that we are dating the pyroclastic deposits directly) and overlaps in age with several ignimbrites both in the Saint Gilles and Saint Pierre areas. Interestingly, Deniel et al. (1992) proposed a similar interpretation but concluded on a significantly younger age (150–100 ka) on the basis of U/Th geochronology, using the Th/U fractionation between whole rock and magnetic minerals from lavas under- and overlying the pyroclastic deposits. Sporadic ash layers found in offshore drill cores suggest a substantial decrease in explosive volcanic activity during the 180–140 kyr interval (Fretzdorff et al., 2000), in agreement with our new dates. Our new, slightly older, age for the “Dalle Soudée” and the explosive events in Saint Gilles and Saint Pierre suggest that the quiescence phase between PN3 and PN4 stages was longer than previously thought, up to 60 kyrs, based on the oldest reported events for PN4 at ca. 140 ka (Salvany et al., 2012; Famin et al., 2022).

The field, petrographic and geochronological data indicate that the end of the PN3 stage corresponds to the growth of a large magma reservoir, which ended with a Plinian-type eruption that covered a large area of the island at 198.8 ± 2.5 ka. The growth of this large reservoir is expected to have taken time, in particular as recharge fluxes decreased during the post-shield phase as the active volcanic center migrated towards Piton de la Fournaise. Such lower fluxes in an otherwise thermally-mature crust, following million years of mafic magmatism, would be favorable to the magma trapping in the upper crust (which due to its lower viscosity would be more accommodating, making space for magma recharge; Townsend et al., 2019), allowing the observed extended differentiation of a parental basaltic magma to form the trachytic melts. Based on the range in bulk rock and groundmass composition, the extreme compositional variability of the crystal cargo in these deposits (Fo_{88} to Fo_{03} olivine, An_{88} to An_{23} plagioclase and Or_{18} and Or_{44} alkali feldspar) and the strong disequilibrium between crystals and the main trachytic groundmass, it seems likely that the entire active crustal plumbing system of Piton des Neiges was drained and disrupted by a significant mafic recharge that led to overpressurization of the reservoir and evacuation of the eruptible parts of it. The occurrence of only few zoned olivine crystals with very short zoning profiles argues for a short interaction between the mafic recharge and the resident, more evolved magmas in the crustal reservoir prior to eruption.

In contrast, the most recent activity (PN4) is characterized by smaller-volume eruptions, whose deposits are constrained to an area much closer to the summit of the edifice. An eruptive unit (Belouve eruption) yielded an age of 44.8 ± 1.3 ka by in-situ $^{238}\text{U}/^{230}\text{Th}$ dating on zircons and of 42.7 ± 3.8 ka by $^{40}\text{Ar}/^{39}\text{Ar}$ dating on single sanidine crystals in the course of the present study. These ages are very close to the K/Ar age of a comenditic cone-sheet in Salazie Cirque (Sa-32: 44.5 ± 1.5 – 40.5 ± 2.0 ka; Gillot and Nativel, 1982) and to a ^{14}C age from charcoal in a paleosol below a trachytic fallout (sample Mu2H: 45.4 ± 1.0 ka; Kluska, 1997) on the western volcano flank. After this event, a set of small volume silicic eruptions have been documented, representing the youngest explosive events of PdN; they include a thick benmoreite lava (36 ± 5 ka; Deniel et al., 1992) in the area of the Forêt de Bébou, a trachytic tephra in the Maïdo area (36.5 ± 2.3 ka; Famin et al., 2022), an aphyric benmoreite lava from coteau Kerveguen (sample 45O1: 29.0 ± 3 ka – 29.5 ± 3 ka; Kluska, 1997), and a trachytic pumice in Belouve dated by ^{14}C in the range 27.0–25.6 ka and 27.5–26.7 ka (dated by Delibrias et al. (1986) and Deniel et al. (1992) and recalibrated by Famin

et al. (2022)). Interestingly, the ages of the two main eruptive stages studied here (ca. 199 and 45 ka) correspond respectively to both a high and low sea level stand (Camoin and Webster, 2015), suggesting that large sea level fluctuations did not play a major role in modulating the explosive activity of Piton des Neiges (Mason et al., 2004; Dumont et al., 2022).

6.3. Age dispersion in young sanidines

In alkalic systems, such as Piton des Neiges, zircons are typically near-solidus minerals; they co-crystallize with sanidine crystals at relatively cold magmatic conditions, estimated for PdN magmas at ~ 875 °C, as magma crystallinity reaches $>30\%$ (Fig. 4). Therefore, when present, such zircons usually record a “crystallization age” that can be interpreted also as the “eruption age” (as seen in Schmitt et al., 2010; Gebauer et al., 2014; Sun et al., 2021). Piton des Neiges is no exception. More striking is the observed large dispersion in the $^{40}\text{Ar}/^{39}\text{Ar}$ dates in all analyzed samples, detected due to the young age of the studied eruptions and the increased sensitivity of modern spectrometers that allow us to resolve age differences not noticeable in the past or in older volcanic events. Interestingly, the recorded dispersion in $^{40}\text{Ar}/^{39}\text{Ar}$ dates is comparable in range to the age results obtained by U-Th disequilibrium dating.

As diffusivity for Ar is considered high in sanidine (e.g., Dodson, 1973; Foland, 1994), they usually reset very rapidly at high temperature (e.g., Singer et al., 1998). Therefore, the interpretation of sanidine Ar ages of volcanic units is based on the assumption that the switch from complete argon loss by diffusion at high temperatures in the magma chamber to low temperatures upon eruption is quick, recording ages that are considered “eruption ages”. Hence, the presence of significant scatter in the $^{40}\text{Ar}/^{39}\text{Ar}$ ages of the sanidines requires the presence of extraneous Ar, either as preserved inherited Ar or as incorporated excess Ar (conventions for terminology of sources of extraneous Ar follow Lanphere and Dalrymple (1976): ^{40}Ar contributing to ages older than expected is called extraneous Ar, a subdivision of extraneous Ar is made into inherited ^{40}Ar that is formed by in-situ decay prior to the event of interest, and excess ^{40}Ar that is parentless ^{40}Ar taken up by the system above the closure temperature).

6.3.1. Excess ^{40}Ar

Excess ^{40}Ar should typically lead, when regressed in isochrons, to an $^{40}\text{Ar}/^{36}\text{Ar}$ intercept that is higher than the atmospheric value (e.g., McDougall and Harrison, 1999; Kelley, 2002). However, the $^{40}\text{Ar}/^{36}\text{Ar}$ intercept for the defined isochrons overlap with accepted atmospheric values of 298.56 ± 0.31 (Lee et al., 2006; Fig. 7A-B), seemingly ruling out the presence of abundant excess ^{40}Ar in those crystals. Analyses that

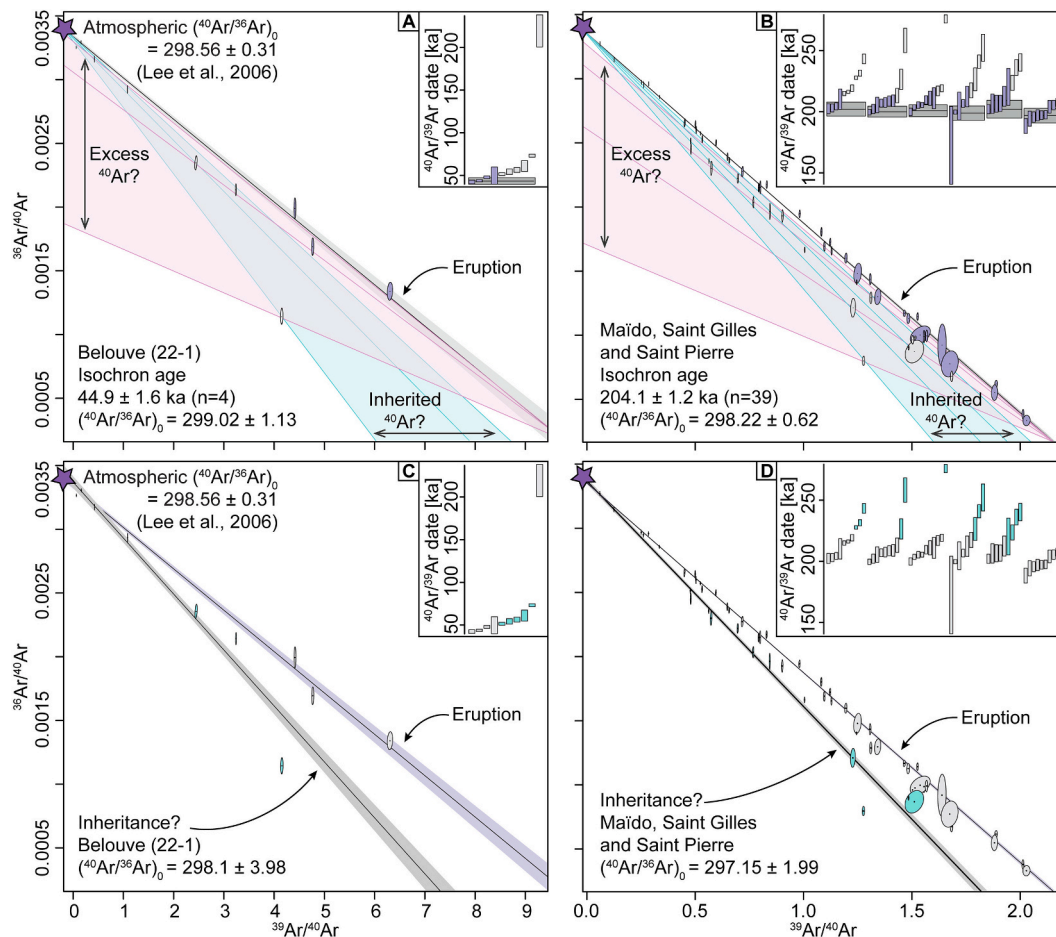


Fig. 7. Inverse isochrons for Belouve (A) and Maïdo, Saint Gilles and Saint Pierre (B). Individual analyses are shown as ellipses with their 2σ uncertainties. Analyses included in isochron construction are shown in purple and correspond to those overlapping with the Bayesian estimate of the eruption age. The regressed isochron indicates $^{40}\text{Ar}/^{36}\text{Ar}$ intercepts concordant with atmospheric composition and ages that correlate with eruption ages calculated via other means. Analyses not included in the isochron (in grey) could describe isochrons with higher $^{40}\text{Ar}/^{36}\text{Ar}$ intercepts (pink area) due to the incorporation of excess Ar into the alkali feldspar, or could define older isochrons with atmospheric intercepts due to the retention of inherited Ar in the crystal prior to eruption (blue area). As an exercise, C and D illustrate isochrons where only older grains are included (in light blue). These older isochrons would also have an $(^{40}\text{Ar}/^{36}\text{Ar})_0$ of atmospheric composition which could indicate retention of inherited Ar inside the crystal at magmatic conditions, with the potential of revealing crystallization ages of alkali feldspar or residence times in the melt. (For interpretation of the references to color in this figure legend, the reader is referred to the web version of this article.)

do not fall on this isochron could also define one that leads to similar estimated eruption ages but with higher intercepts, advocating for the presence of excess Ar in some crystals (shown in pink shades in Fig. 7A-B). Although it is not impossible that some excess Ar is present in small quantities in our PdN samples, we do not consider that it significantly contributes to the scatter towards old dates. This is consistent with the detailed inspection of the alkali feldspars we performed prior to analysis that did not reveal the presence of melt/fluid inclusions as potential hosts of excess argon. Additionally, for ^{40}Ar to enter the crystal lattice from the surrounding melt, it needs to overcome the energetic barrier imposed by the strong preference of ^{40}Ar to partition into the melt/fluid phase instead of the crystal lattice (Foland, 1994; Clay et al., 2011).

6.3.2. Inherited ^{40}Ar

Assuming that excess ^{40}Ar does not account for the older sanidine dates, then radiogenic Ar must have been kept in the crystal over 80 kyr under magma chamber P-T conditions. In that case, older dates would define isochrons with atmospheric $^{40}\text{Ar}/^{36}\text{Ar}$ intercepts that are older than the youngest population of crystals (shown in blue shades in Fig. 7A-B) and that could represent minimum magma residence times or sanidine crystallization ages. As an exercise, we built an isochron including only those grains that result in $^{40}\text{Ar}/^{39}\text{Ar}$ dates older than the calculated Bayesian eruption age (shown in light blue in Fig. 7C-D). Consequently, isochrons for both Belouve and Maïdo, Saint Gilles and Saint Pierre are older but indicate $^{40}\text{Ar}/^{36}\text{Ar}$ intercepts that still overlap with atmospheric compositions, illustrating that if only these grains were to be analyzed, an older isochron with no evidence of incorporation of excess Ar could be built.

A key challenge to the inherited Ar hypothesis is that the Ar closure temperature in alkali feldspar varies from 200 to a max of ~ 400 °C (Cassata and Renne, 2013; Reiners et al., 2017). Using published Ar diffusion data at magmatic temperatures (> 700 °C), the crystals should have been reset within < 100 years (Andersen et al., 2017). Therefore, in order to preserve inherited (old) argon in the structure of the sanidine for tens of thousands of years, either the temperature of storage was extremely low (subsolidus; e.g., Andersen et al., 2017; Mucek et al., 2021) and the entrainment of those sanidines in the hot, erupted portion of the magma reservoir happened very shortly prior to eruption (Gillespie et al., 1982; De Beni et al., 2005; Renne et al., 2012) or diffusivities of Ar atoms are much slower than expected. In the studied samples, alkali feldspar is found isolated mostly as euhedral to subhedral crystals, surrounded by groundmass glass. Therefore, we assume they were part of the eruptible magma and not xenocrysts entrained during or near eruption from the cold surroundings. If the cold surroundings were to be mobilized during eruption, we expect to find syenitic blocks in the deposits; such blocks were not observed in any sampled location or analyzed hand specimen.

6.3.2.1. Retention of inherited ^{40}Ar in alkali feldspar at magmatic conditions. Our observations propose a new challenge in view of the current understanding of Ar diffusion in alkali feldspar. The fundamental assumption in Ar diffusion models is that the boundary condition is set to an Ar concentration of zero at the crystal surface (Crank, 1975; Dodson, 1973; Lee, 1995), thus creating a strong concentration gradient and, hence allowing diffusive transport. However, in the magma, especially in a hotspot related mantle plume, this requirement cannot be met as the concentration of Ar in the melt may not be zero. Noble gas experiments have indicated that a basaltic melt could contain around 400 ppm of dissolved Ar at 2 kbar, while in a rhyolitic melt Ar concentration could increase up to 1000 ppm in the shallow crust at magmatic temperatures (Paonita, 2005). If a melt contains a finite concentration of K_2O , and is a uniform medium, diffusion loss from the melt is proportional to the radius of the magma body. When the radius of the magma body is large, and the diffusivity decreases with temperature, Ar accumulation in the magma is to be expected.

As a result, three scenarios could be explored if the concentration of ^{40}Ar in the melt ($^{40}\text{Ar}_{\text{melt}}$) is higher than, (nearly-) equal to, or lower than the concentration of ^{40}Ar in the alkali feldspar ($^{40}\text{Ar}_{\text{Kfsp}}$; Fig. 8A, B and C, respectively). From the moment a K-feldspar forms in the melt at temperatures that are above its closure temperature ($t = 0$), and continues growing ($t = X$), it could encounter any of these three scenarios while its structurally bound ^{40}K produces in-situ radiogenic ^{40}Ar . If $^{40}\text{Ar}_{\text{melt}} > ^{40}\text{Ar}_{\text{Kfsp}}$, a concentration gradient could drive ^{40}Ar to be incorporated into the crystal, resulting in an excess ^{40}Ar diffusion profile in the feldspar at the moment of eruption and overestimated $^{40}\text{Ar}/^{39}\text{Ar}$ dates with no geological relevance (Fig. 8A). However, to move from the melt into the crystal lattice, Ar atoms would need to overcome the energy barrier at the crystal surface. Such consideration suggests that Ar diffusion into the sanidine crystal would only take place when the Ar overpressure in the melt is significant. In contrast, if $^{40}\text{Ar}_{\text{melt}} < ^{40}\text{Ar}_{\text{Kfsp}}$, an inverse concentration gradient would form, driving the diffusive loss of ^{40}Ar out of the feldspar into the melt (Fig. 8C). Under such conditions, ^{40}Ar produced by in-situ decay of ^{40}K from the crystal would be lost before eruption, resetting the K-Ar system and recording only the time elapsed since the crystal cooled below its closure temperature (e.g., at $t = \text{eruption}$). Consequently, the feldspar population in an erupted unit might record $^{40}\text{Ar}/^{39}\text{Ar}$ dates that are consistent with eruption ages and show diffusion profiles typical of ^{40}Ar loss (e.g., Phillips and Matchan, 2013). However, if $^{40}\text{Ar}_{\text{melt}} \approx ^{40}\text{Ar}_{\text{Kfsp}}$ no significant concentration gradient would form and the diffusion of ^{40}Ar in or out of the crystal would be hampered. We would then expect a finite concentration difference window, where the low concentration gradient in combination with the energy barrier at the crystal surface would prevent Ar transport into or out of the crystals. In that case, ^{40}Ar formed in-situ by radioactive decay since the formation of the crystal would remain inside the crystal, recording crystallization ages with homogenous Ar concentrations (Fig. 8B).

In limited number of cases, profiles of excess argon into minerals have been documented or modeled (e.g., Wijbrans and McDougall, 1988; Reddy et al., 1996), whereas diffusive loss patterns are far more abundant (e.g., Turner et al., 1966; Lovera et al., 1989; Wartho et al., 1999; Cassata and Renne, 2013). However, no careful evaluation of the diffusive behavior of Ar in feldspar has been studied under conditions where the crystal is surrounded by a similarly-Ar-rich medium. Hence, on the basis of

- i) the lack of evidence for entrainment of the subsolidus host during eruption that could have provided old xenocrystic sanidines,
- ii) the careful inspection of the dated crystals to account for gem-quality grains free of inclusions,
- iii) the reported high fluxes of CO_2 and noble gases on La Réunion even during phases of quiescence (e.g., Liuzzo et al., 2015; Bou-doire et al., 2020), and
- iv) the extremely low partition coefficients for Ar between crystal and melt/fluid (Foland, 1994; Clay et al., 2011),

we propose that the observed spread towards older dates in our $^{40}\text{Ar}/^{39}\text{Ar}$ dates is dominantly due to the retention of inherited ^{40}Ar into the sanidine structure prior to eruption.

While some *syn*-eruptive degassing will lower the Ar content of the matrix melt upon eruption (e.g., Fig. 8; $t = \text{eruption}$), the rapid ascent rate from the reservoir to the surface (as inferred from the explosivity of the eruption and the very narrow and sharp zoning profiles in olivine rims) would have strongly limited the *syn*-eruptive degassing interval. The ascent of magma with concomitant cooling would occur in a matter of days or weeks, whereas diffusive loss of argon from the sanidine crystal lattice in the pertinent temperature range would take years to 10^5 's of years. Hence, we suggest that the relatively high ambient Ar concentration of the melt surrounding the alkali feldspar slowed down (or even hampered) the diffusion of Ar out of the crystal lattice by decreasing the effective concentration gradients over the crystal-melt

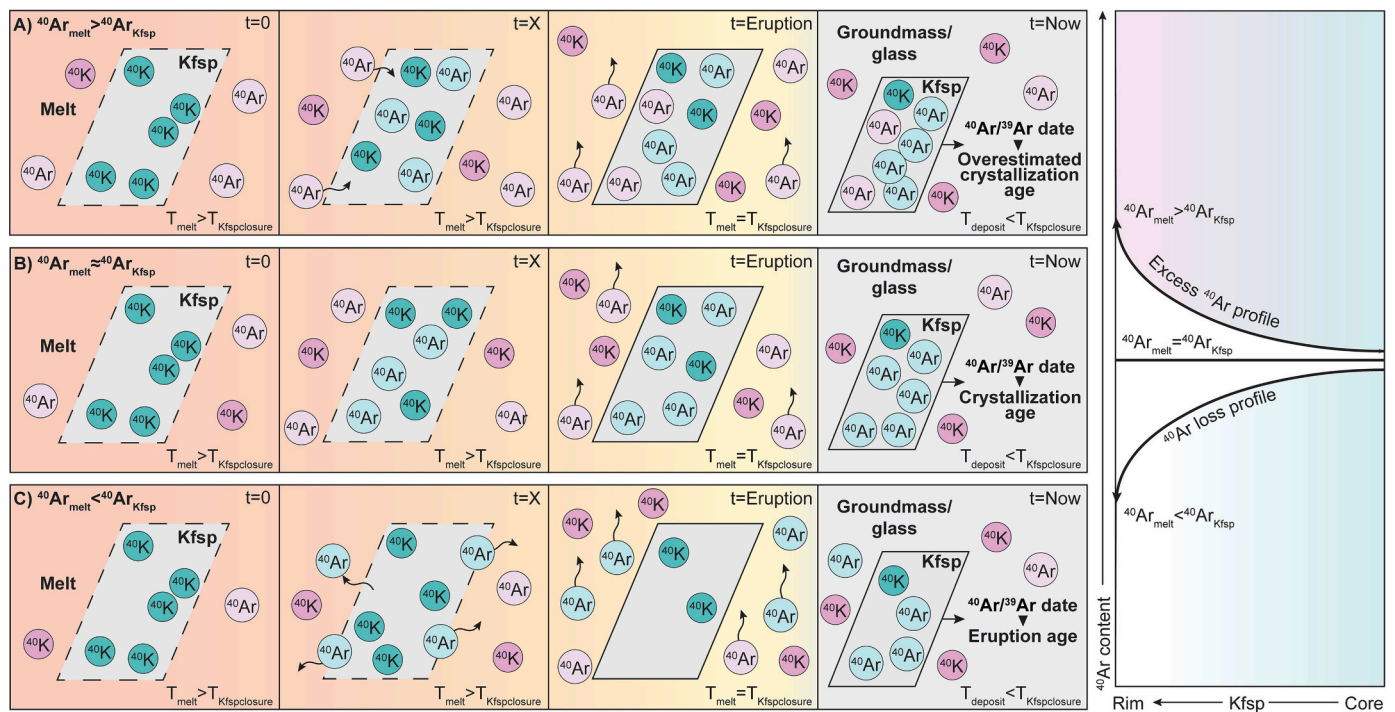


Fig. 8. Schematic representation of argon diffusion between alkali feldspar (Kfsp) and melt under conditions of A) higher ^{40}Ar content in the melt relative to the crystal, B) nearly-equal ^{40}Ar contents between the melt and the crystal, and C) higher ^{40}Ar concentrations in the crystal relative to the surrounding melt. These scenarios are explored along a cooling interval from the time of feldspar formation ($t = 0$) and growth/residence ($t = X$) to the time of eruption ($t = \text{eruption}$) and its resulting $^{40}\text{Ar}/^{39}\text{Ar}$ date and geological relevance. ^{40}K and ^{40}Ar are represented as color-coded circles relative to their source (pink shades refer to ^{40}K and ^{40}Ar (parentless) dissolved in the melt; blue-green shades refer to the structural ^{40}K in the feldspar and its in situ decay to ^{40}Ar). Curved arrows in $t = \text{eruption}$ indicate the partial loss of ^{40}Ar from the melt due to syn-eruptive degassing. The resulting diffusion profiles in the feldspar from core to rim for each scenario are presented on the right. (For interpretation of the references to color in this figure legend, the reader is referred to the web version of this article.)

boundaries, therefore promoting the retention of radiogenic Ar even at magma chamber P-T conditions.

6.3.3. Considerations from zircon geochemistry

The chemical variability of zircon crystals further supports a relatively long residence time in the upper crustal magma reservoir. Consistent variations in trace element contents between core, rims and outermost rims within the crystal population, indicate that the zircon grains crystallized during a prolonged interval in response to changes in melt chemistry, temperature and possibly oxidation state. Zircon cores crystallized from a magma with higher U/Th ratios, Nb concentrations, and Ce anomalies (Ce/Ce^*) than the rims (Fig. 6C-D), suggesting progressive differentiation accompanied by the fractionation of amphibole + biotite \pm Fe-Ti oxide, and possibly a progressive change towards more reducing conditions (Pearce and Norry, 1979; Trail et al., 2012). However, the link between Ce anomalies and oxidation state should be stated with caution due to the dependency of the Ce anomaly on changes in temperature, melt chemistry and oxidation state (Loader et al., 2022). Additionally, overlapping Ti-in-zircon temperatures with estimated crystallization temperatures of alkali feldspar (Fig. 4) indicate that sanidine and zircon co-crystallized in this system.

In summary, we argue that the complex Ar age patterns in the PdN alkali feldspar result from the presence of inherited Ar in the crystals, owing to protracted crystallization in a long-lived magma reservoir containing significant ambient argon. Specifically, age dispersion in our data suggests that the magma chamber that fed the Plinian-type event was able to punctually crystallize sanidine over a period of at least 80 kyr. The same applies for the less voluminous dome forming eruption during PN4, where the excess age dispersion in the sanidine population could allow for at least 30 kyr of residence in the magma chamber. Retention of inherited Ar in the most retentive parts of the crystals has been previously suggested (Van den Bogaard and Schirnick, 1995;

Bachmann et al., 2007), although clear explanations for this observation were lacking. Several recent studies also documented complex Ar age spectra in volcanic units (e.g., Bachmann et al., 2010; Phillips and Matchan, 2013; Ellis et al., 2017; Morgan et al., 2019; Van Zalinge et al., 2022), and diffusion of elements (including small ions and noble gases) appears more complex than previously thought (e.g., multi-species diffusion on multiple different pathways; Baxter, 2010; Dohmen et al., 2010; Sliwinski et al., 2018; Bloch et al., 2020; Neukampf et al., 2022), highlighting the need for a better understanding of Ar diffusion in feldspar under different P-T-a(Ar) conditions.

6.4. Eruptive potential of Piton des Neiges

Progressively less voluminous eruptions of compositionally more evolved magmas of Piton des Neiges from the start of the PN3 stage indicate that the PdN magma reservoir has been shrinking, probably due to the decrease in flux of mafic magma, as it shifted to feed the basaltic volcanism of PdF. However, geophysical observations of deep magmatic activity around 35 km below sea level between the two volcanoes (Michon et al., 2015; Boudoire et al., 2017) argues for a continuing deep magma supply towards Piton des Neiges. Furthermore, long repose periods are recurrent, considering the 100 kyrs quiescence between PN2 and PN3 stages (McDougall, 1971), our redefined 60 kyrs gap between PN3 and PN4 stages and other shorter periods reviewed by Salvany et al. (2012). Following the most recent eruptive record (ca. 27 ka) and the defined geochemical evolution of this volcano, future eruptions cannot be excluded. If following the same trend, they will be less voluminous but more evolved. Although small volume can be expected, silica- and volatile-rich melts with high viscosities can result in highly explosive events (e.g. Rocher, 1988; Kieffer, 1989; Kluska, 1997). This rare, but hazardous eruptive style observed in Piton des Neiges poses a significant risk in this populated island and requires monitoring as well as further

efforts to better understand its current magmatic activity.

7. Conclusions and outlook

Piton des Neiges volcanism has evolved from basaltic to trachytic-rhyolitic since it entered its post-shield stage as the center of volcanic activity drifted to build Piton de la Fournaise at about 0.53 Ma. Continuous but lower magma fluxes in the mature crustal plumbing system have maintained a magmatic reservoir beneath Piton des Neiges, allowing extensive fractionation of the pre-existent basaltic magmas to generate more differentiated compositions and maintaining eruptible pockets of more silicic melt available to feed more evolved alkalic volcanism from Piton des Neiges. Several trachytic pyroclastic deposits with ignimbrite packages of up to 15 m height, regarded as individual eruptive events, are found in the areas of Maïdo, Saint Gilles and Saint Pierre. We report whole rock and mineral chemistry in combination with new high precision $^{40}\text{Ar}/^{39}\text{Ar}$ dates in sanidine that allow us to correlate these pyroclastic sequences as part of a single plinian-type eruption (the Dalle Soudée eruption) that occurred at 198.8 ± 2.5 ka and covered a large part of the island. A rapid, hot and voluminous mafic recharge may have triggered the large explosive event characterized by a strong open system behavior that disrupted the entire plumbing system, as indicated by the large disequilibrium between the erupted groundmass and the crystal cargo. Our results indicate that the dormancy phase between PN3 and PN4 stages was up to 60 kyr, ca. 20 kyr longer than previously thought. Younger explosive volcanism has also been recorded. Here, we geochemically characterize and provide absolute eruption ages of a block and ash flow deposit found near the summit in Belouve at 42.7 ± 3.8 ka. This deposit represents pyroclastic density currents that could have formed due to the collapse of a growing lava dome, a hazardous eruptive style and yet not recognized for Piton des Neiges. Importantly, the occurrence of repose periods of up to 100 kyr during its eruptive history and the reported deep magmatic activity between Piton des Neiges and Piton de la Fournaise lead us to suggest that active magma supply towards Piton des Neiges and future volcanism should not be discarded.

Furthermore, our single crystal $^{40}\text{Ar}/^{39}\text{Ar}$ dates in sanidine show a spread towards older dates that covers in total ~ 80 kyr between the youngest and oldest dated crystal. Such spread is not common in volcanic alkali feldspars due to its low closure temperature, and it could be due to the incorporation of excess or inherited argon into the apparently older crystals. Based on the careful inspection prior analyses to select only gem-quality crystals without inclusions that could contribute to excess Ar, the lack of evidence for the entrainment of xenocrystic sanidine, and the low Ar partition coefficient between crystal and melt, we suggest that the age dispersion in sanidine might not be related to the incorporation of excess Ar into the crystal prior eruption. Instead, we propose that the presence of Ar in the surrounding melt, supported by reported high fluxes of noble gases on La Réunion, limited the formation of a strong concentration gradient and hampered the diffusion of ^{40}Ar out of the sanidine. Consequently, ^{40}Ar produced by in-situ radioactive decay was retained inside the crystal at magma chamber conditions allowing us to provide minimum crystallization ages. To better explore this scenario, future work should focus on modelling the Ar diffusion in sanidine with boundary conditions different than zero. Moreover, additional $^{40}\text{Ar}/^{39}\text{Ar}$ dating on single sanidine or other mineral phases or groundmass glass using the step heating technique could provide further clarifications for the observed large dispersion in sanidine $^{40}\text{Ar}/^{39}\text{Ar}$ dates.

Declaration of Competing Interest

The authors declare that they have no known competing financial interests or personal relationships that could have appeared to influence the work reported in this paper.

Data availability

The data used for this research has been shared in the supplementary files

Acknowledgments

We extend our gratitude to Dr. Ben Ellis for his continued support and encouraging discussions during the development of this project. We also thank Dr. Julia Neukampf for her help during EPMA analyses and Dr. Marcel Guillong for his assistance with LA-ICP-MS analyses and insightful discussions. We are thankful for the constructive reviews by Allan S. Gomes and one anonymous reviewer whose comments and suggestions helped us improve the quality of the manuscript. We also would like to thank the Grubenmann-Burri-Fonds, ETH Zürich and the Swiss SNF grant 200020_207358 for financially supporting this study.

Appendix A. Supplementary data

Supplementary data to this article can be found online at <https://doi.org/10.1016/j.chemgeo.2023.121539>.

References

- Albarède, F., Luais, B., Fitton, G., Semet, M., Kaminski, E., Upton, B.G.J., Bachèlery, P., Cheminée, J.L., 1997. The geochemical regimes of Piton de la Fournaise volcano (Réunion) during the last 530 000 years. *J. Petrol.* 38 (2), 171–201.
- Andersen, N.L., Singer, B.S., Jicha, B.R., Beard, B.L., Johnson, C.M., Licciardi, J.M., 2017. Pleistocene to Holocene growth of a large upper crustal rhyolitic magma reservoir beneath the active Laguna del Maule volcanic field, Central Chile. *J. Petrol.* 58 (1), 85–114.
- Bachmann, O., Oberli, F., Dungan, M.A., Meier, M., Mundil, R., Fischer, H., 2007. $^{40}\text{Ar}/^{39}\text{Ar}$ and U–Pb dating of the Fish Canyon magmatic system, San Juan volcanic field, Colorado: evidence for an extended crystallization history. *Chem. Geol.* 236 (1–2), 134–166.
- Bachmann, O., Schoene, B., Schnyder, C., Spikings, R., 2010. The $^{40}\text{Ar}/^{39}\text{Ar}$ and U/Pb dating of young rhyolites in the Kos-Nisyros volcanic complex, Eastern Aegean Arc, Greece: Age discordance due to excess ^{40}Ar in biotite. *Geochem. Geophys. Geosyst.* 11 (8).
- Baksi, A.K., Hoffman, K.A., 2000. On the age and morphology of the Réunion event. *Geophys. Res. Lett.* 27 (18), 2997–3000.
- Baksi, A.K., Hoffman, K.A., McWilliams, M., 1993. Testing the accuracy of the geomagnetic polarity time-scale (GPTS) at 2–5 Ma, utilizing $^{40}\text{Ar}/^{39}\text{Ar}$ incremental heating data on whole-rock basalts. *Earth Planet. Sci. Lett.* 118 (1–4), 135–144.
- Basu, A.R., Chakrabarty, P., Szymanowski, D., Ibañez-Mejía, M., Schoene, B., Ghosh, N., Georg, R.B., 2020. Widespread silicic and alkaline magmatism synchronous with the Deccan Traps flood basalts, India. *Earth Planet. Sci. Lett.* 552, 116616.
- Baxter, E.F., 2010. Diffusion of noble gases in minerals. *Rev. Mineral. Geochem.* 72 (1), 509–557.
- Bénard, B., Famin, V., Agrinier, P., Aunay, B., Lebeau, G., Sanjuan, B., Vimeux, F., Bardoux, G., Dezayes, C., 2020. Origin and fate of hydrothermal fluids at Piton des Neiges volcano (Réunion Island): a geochemical and isotopic (O, H, C, Sr, Li, Cl) study of thermal springs. *J. Volcanol. Geotherm. Res.* 392, 106682.
- Berthod, C., Michon, L., Famin, V., Welsch, B., Bachèlery, P., Bascou, J., 2020. Layered gabbros and peridotites from Piton des Neiges volcano, La Réunion Island. *J. Volcanol. Geotherm. Res.* 405, 107039.
- Bloch, E.M., Jollands, M.C., Devoir, A., Bouvier, A.S., Ibañez-Mejía, M., Baumgartner, L.P., 2020. Multispecies diffusion of yttrium, rare earth elements and hafnium in garnet. *J. Petrol.* 61 (7), ega055.
- Boehnke, P., Watson, E.B., Trail, D., Harrison, T.M., Schmitt, A.K., 2013. Zircon saturation re-revisited. *Chem. Geol.* 351, 324–334.
- Boudoire, G., Liuzzo, M., Di Muro, A., Ferrazzini, V., Michon, L., Grassa, F., Derrien, A., Villeneuve, N., Bourdeu, A., Brunet, C., Giudice, G., Gurrieri, S., 2017. Investigating the deepest part of a volcano plumbing system: evidence for an active magma path below the western flank of Piton de la Fournaise (La Réunion Island). *J. Volcanol. Geotherm. Res.* 341, 193–207.
- Boudoire, G., Rizzo, A.L., Arienzo, I., Di Muro, A., 2020. Paroxysmal eruptions tracked by variations of helium isotopes: inferences from Piton de la Fournaise (La Réunion island). *Sci. Rep.* 10 (1), 1–16.
- BRGM (Cartographe), 2006. Carte Géologique De La Réunion. 1:100.000.
- Camoin, G.F., Webster, J.M., 2015. Coral reef response to Quaternary Sea-level and environmental changes: state of the science. *Sedimentology* 62 (2), 401–428.
- Cassata, W.S., Renne, P.R., 2013. Systematic variations of argon diffusion in feldspars and implications for thermochronometry. *Geochim. Cosmochim. Acta* 112, 251–287.
- Clay, P.L., Kelley, S.P., Sherlock, S.C., Barry, T.L., 2011. Partitioning of excess argon between alkali feldspars and glass in a young volcanic system. *Chem. Geol.* 289 (1–2), 12–30.
- Connor, C.B., McBirney, A.R., Furlan, C., 2006. What Is the Probability of Explosive Eruption at a Long-Dormant Volcano?.

- Crank, J., 1975. *The Mathematics of Diffusion*. Oxford. Clarendon, England.
- De Beni, E., Wijbrans, J.R., Branca, S., Coltelli, M., Groppelli, G., 2005. New results of ⁴⁰Ar/³⁹Ar dating constrain the timing of transition from fissure-type to central volcanism at Mount Etna (Italy). *Terra Nova* 17 (3), 292–298.
- de Voogd, B., Palomé, S.P., Hirn, A., Charvis, P., Gallart, J., Rousset, D., Dañoibeitia, J., Perroud, H., 1999. Vertical movements and material transport during hotspot activity: Seismic reflection profiling offshore La Réunion. *J. Geophys. Res. Solid Earth* 104 (B2), 2855–2874.
- Delibrias, G., Guillier, M.T., Labeysrie, J., 1986. Gif natural radiocarbon measurements X. *Radiocarbon* 28 (1), 9–68.
- Deniel, C., Kieffer, G., Lecointre, J., 1992. New ²³⁰Th-²³⁸U and ¹⁴C age determinations from Piton des Neiges volcano, Reunion—a revised chronology for the Differentiated Series. *J. Volcanol. Geotherm. Res.* 51 (3), 253–267.
- Dodson, M.H., 1973. Closure temperature in cooling geochronological and petrological systems. *Contrib. Mineral. Petrol.* 40 (3), 259–274.
- Dohmen, R., Kasemann, S.A., Coogan, L., Chakraborty, S., 2010. Diffusion of Li in olivine. Part I: experimental observations and a multi species diffusion model. *Geochim. Cosmochim. Acta* 74 (1), 274–292.
- Dumont, S., Petrosino, S., Neves, M.C., 2022. On the link between global volcanic activity and global mean sea level. *Front. Earth Sci.* 10, 845511.
- Duncan, R.A., Backman, J., Peterson, L., Party, T.S.S., 1989. Reunion hotspot activity through tertiary time: initial results from the ocean drilling program, leg 115. *J. Volcanol. Geotherm. Res.* 36 (1–3), 193–198.
- Duputel, Z., Ferrazzini, V., Lengliné, O., Michon, L., Fontaine, F.R., Massin, F., 2021. Seismicity of La Réunion island. *Comptes Rendus. Géoscience* 353 (S1), 237–255.
- Ellis, B.S., Mark, D.F., Troch, J., Bachmann, O., Guillong, M., Kent, A.J., von Quadt, A., 2017. Split-grain ⁴⁰Ar/³⁹Ar dating: Integrating temporal and geochemical data from crystal cargoes. *Chem. Geol.* 457, 15–23.
- Famin, V., Paquez, C., Danišik, M., Gardiner, N.J., Michon, L., Kirkland, C.L., Berthod, K. C., Friedrichs, B., Schmitt, A.K., Monie, P., 2022. Multitechnique geochronology of intrusive and explosive activity on Piton des Neiges volcano, Réunion Island. *Geochem. Geophys. Geosyst.* 23 (5), e2021GC001214.
- Ferry, J.M., Watson, E.B., 2007. New thermodynamic models and revised calibrations for the Ti-in-zircon and Zr-in-rutile thermometers. *Contrib. Mineral. Petrol.* 154 (4), 429–437.
- Fisk, M.R., Upton, B.G.J., Ford, C.E., White, W.M., 1988. Geochemical and experimental study of the genesis of magmas of Reunion Island, Indian Ocean. *J. Geophys. Res. Solid Earth* 93 (B5), 4933–4950.
- Foland, K.A., 1994. Argon diffusion in feldspars. In: *Feldspars and their Reactions*. Springer, Dordrecht, pp. 415–447.
- Fretzdorff, S., Paterne, M., Stoffers, P., Ivanova, E., 2000. Explosive activity of the Reunion Island volcanoes through the past 260,000 years as recorded in deep-sea sediments. *Bull. Volcanol.* 62 (4), 266–277.
- Gayer, E., Michon, L., Louvat, P., Gaillardet, J., 2019. Storm-induced precipitation variability control of long-term erosion. *Earth Planet. Sci. Lett.* 517, 61–70.
- Gebauer, S.K., Schmitt, A.K., Pappalardo, L., Stockli, D.F., Lovera, O.M., 2014. Crystallization and eruption ages of Breccia Museo (Campi Flegrei caldera, Italy) plutonic clasts and their relation to the Campanian ignimbrite. *Contrib. Mineral. Petrol.* 167 (1), 1–18.
- Ghiorso, M.S., Gualda, G.A., 2015. An H₂O–CO₂ mixed fluid saturation model compatible with rhyolite-MELTS. *Contrib. Mineral. Petrol.* 169 (6), 1–30.
- Gillespie, A.R., Huneke, J.C., Wasserburg, G.J., 1982. An assessment of ⁴⁰Ar-³⁹Ar dating of incompletely degassed xenoliths. *J. Geophys. Res. Solid Earth* 87 (B11), 9247–9257.
- Gillot, P.Y., Nativel, P., 1982. K-Ar chronology of the ultimate activity of Piton des Neiges volcano, Reunion island, Indian ocean. *J. Volcanol. Geotherm. Res.* 13 (1–2), 131–146.
- Gillot, P.Y., Nativel, P., 1989. Eruptive history of the Piton de la Fournaise volcano, Réunion island, Indian Ocean. *J. Volcanol. Geotherm. Res.* 36 (1–3), 53–65.
- Gillot, P.Y., Lefevre, J.C., Nativel, P.E., 1994. Model for the structural evolution of the volcanoes of Réunion Island. *Earth Planet. Sci. Lett.* 122 (3–4), 291–302.
- Giordano, D., Ardia, P., Romano, C., Dingwell, D.B., Di Muro, A., Schmidt, M.W., Hess, K. U., 2009. The rheological evolution of alkaline Vesuvius magmas and comparison with alkaline series from the Phlegrean Fields, Etna, Stromboli and Teide. *Geochim. Cosmochim. Acta* 73 (21), 6613–6630.
- Gualda, G.A., Ghiorso, M.S., Lemons, R.V., Carley, T.L., 2012. Rhyolite-MELTS: a modified calibration of MELTS optimized for silica-rich, fluid-bearing magmatic systems. *J. Petrol.* 53 (5), 875–890.
- Guillong, M., Sliwinski, J.T., Schmitt, A., Forni, F., Bachmann, O., 2016. U-Th zircon dating by laser ablation single collector inductively coupled plasma-mass spectrometry (LA-ICP-MS). *Geostand. Geoanal. Res.* 40 (3), 377–387.
- Hayden, L.A., Watson, E.B., 2007. Rutile saturation in hydrous siliceous melts and its bearing on Ti-thermometry of quartz and zircon. *Earth Planet. Sci. Lett.* 258 (3–4), 561–568.
- Keller, C.B., Schoene, B., Samperton, K.M., 2018. A stochastic sampling approach to zircon eruption age interpretation. *Geochem. Perspect. Lett. (Online)* 8 (LLNL-JRNL-738859).
- Kelley, S., 2002. K-Ar and Ar-Ar dating. *Rev. Mineral. Geochem.* 47 (1), 785–818.
- Kieffer, G., 1989. La formation des cirques du massif du Piton des Neiges (La Réunion) (the formation of the volcanic cirques in the Reunion island). *Bulletin de l'Association de géographes français* 66 (5), 361–370.
- Kieffer, G., Gillot, P.Y., Cornette, Y., Germanaz, C., Nativel, P., 1993. An exceptional eruptive phase in the recent history of Piton des Neiges (Reunion Island): the eruption of “the welded slab”. In: *Proceedings of the Academy of Sciences Series II*, 317, pp. 835–842.
- Kluska, J.M., 1997. *Magmatic and morpho-structural evolution of the Piton des Neiges over the last 500,000 years* (Doctoral dissertation, Paris 11).
- Lanphere, M.A., Dalrymple, G.B., 1976. Identification of excess ⁴⁰Ar by the ⁴⁰Ar/³⁹Ar age spectrum technique. *Earth Planet. Sci. Lett.* 32 (2), 141–148.
- Laumonier, M., Karakas, O., Bachmann, O., Gaillard, F., Lukács, R., Seghedi, I., Menand, T., Harangi, S., 2019. Evidence for a persistent magma reservoir with large melt content beneath an apparently extinct volcano. *Earth Planet. Sci. Lett.* 521, 79–90.
- Lee, J.K., 1995. Multipath diffusion in geochronology. *Contrib. Mineral. Petrol.* 120 (1), 60–82.
- Lee, J.Y., Marti, K., Severinghaus, J.P., Kawamura, K., Yoo, H.S., Lee, J.B., Kim, J.S., 2006. A redetermination of the isotopic abundances of atmospheric Ar. *Geochim. Cosmochim. Acta* 70 (17), 4507–4512.
- Lénat, J.F., 2016. *Construction of La Réunion*. In: *Active Volcanoes of the Southwest Indian Ocean*. Springer, Berlin, Heidelberg, pp. 31–44.
- Liebske, C., 2015. iSpectra: an open source toolbox for the analysis of spectral images recorded on scanning electron microscopes. *Microsc. Microanal.* 21 (4), 1006–1016.
- Liuzzo, M., Di Muro, A., Giudice, G., Michon, L., Ferrazzini, V., Guerrieri, S., 2015. New evidence of CO₂ soil degassing anomalies on Piton de la Fournaise volcano and the link with volcano tectonic structures. *Geochem. Geophys. Geosyst.* 16 (12), 4388–4404.
- Loader, M.A., Nathwani, C.L., Wilkinson, J.J., Armstrong, R.N., 2022. Controls on the magnitude of Ce anomalies in zircon. *Geochim. Cosmochim. Acta* 328, 242–257.
- Loucks, R.R., Fiorentini, M.L., Henríquez, G.J., 2020. New magmatic oxybarometer using trace elements in zircon. *J. Petrol.* 61 (3), egaa034.
- Lovera, O.M., Richter, F.M., Harrison, T.M., 1989. The ⁴⁰Ar/³⁹Ar thermochronometry for slowly cooled samples having a distribution of diffusion domain sizes. *J. Geophys. Res. Solid Earth* 94 (B12), 17917–17935.
- Lukács, R., Guillong, M., Bachmann, O., Fodor, L., Harangi, S., 2021. Tephrostratigraphy and magma evolution based on combined Zircon trace element and U-Pb Age data: fingerprinting miocene silicic pyroclastic rocks in the Pannonian Basin. *Front. Earth Sci.* 9, 615768.
- Mahoney, J.J., Duncan, R.A., Khan, W., Gnos, E., McCormick, G.R., 2002. Cretaceous volcanic rocks of the south Tethyan suture zone, Pakistan: implications for the Réunion hotspot and Deccan Traps. *Earth Planet. Sci. Lett.* 203 (1), 295–310.
- Martí, J., Mitjavila, J., Araña, V., 1994. Stratigraphy, structure and geochronology of the Las Cañadas caldera (Tenerife, Canary Islands). *Geol. Mag.* 131 (6), 715–727.
- Marty, B., Meynier, V., Nicolini, E., Griesshaber, E., Toutain, J.P., 1993. Geochemistry of gas emanations: a case study of the Réunion Hot Spot, Indian Ocean. *Appl. Geochem.* 8 (2), 141–152.
- Mason, B.G., Pyle, D.M., Dade, W.B., Jupp, T., 2004. Seasonality of volcanic eruptions. *J. Geophys. Res. Solid Earth* 109 (B4).
- McDougall, I., 1971. The geochronology and evolution of the young volcanic island of Réunion, Indian Ocean. *Geochim. Cosmochim. Acta* 35 (3), 261–288.
- McDougall, I., Harrison, T.M., 1999. *Geochronology and Thermochronology by the ⁴⁰Ar/³⁹Ar Method*. Oxford University Press.
- McDougall, I., Watkins, N.D., 1973. Age and duration of the Réunion geomagnetic polarity event. *Earth Planet. Sci. Lett.* 19 (4), 443–452.
- Michon, L., Ferrazzini, V., Di Muro, A., Villeneuve, N., Famin, V., 2015. Rift zones and magma plumbing system of Piton de la Fournaise volcano: how do they differ from Hawaii and Etna? *J. Volcanol. Geotherm. Res.* 303, 112–129.
- Mollo, S., Masotta, M., Forni, F., Bachmann, O., De Astis, G., Moore, G., Scarlato, P., 2015. A K-feldspar–liquid hygrometer specific to alkaline differentiated magmas. *Chem. Geol.* 392, 1–8.
- Molnár, K., Lukács, R., Dunkl, I., Schmitt, A.K., Kiss, B., Seghedi, I., Szepesi, J., Harangi, S., 2019. Episodes of dormancy and eruption of the late Pleistocene Ciomadul volcanic complex (Eastern Carpathians, Romania) constrained by zircon geochronology. *J. Volcanol. Geotherm. Res.* 373, 133–147.
- Morgan, W.J., 1981. 13. Hotspot tracks and the opening of the Atlantic and Indian Oceans. *The Oceanic Lithosphere* 7.
- Morgan, L.E., Johnstone, S.A., Gilmer, A.K., Cosca, M.A., Thompson, R.A., 2019. A supervolcano and its sidekicks: a 100 ka eruptive chronology of the fish Canyon Tuff and associated units of the La Garita magmatic system, Colorado, USA. *Geology* 47 (5), 453–456.
- Mucek, A.E., Danišik, M., de Silva, S.L., Miggins, D.P., Schmitt, A.K., Pratomio, I., Koppers, A., Gillespie, J., 2021. Resurgence initiation and subsolidus eruption of cold carapace of warm magma at Toba Caldera, Sumatra. *Commun. Earth Environ.* 2 (1), 185.
- Nativel, P., 1978. *Reunion Volcanoes: Petrology* (Doctoral dissertation).
- Nauret, F., Famin, V., Vlastélic, I., Gannoun, A., 2019. A trace of recycled continental crust in the Réunion hotspot. *Chem. Geol.* 524, 67–76.
- Neukampf, J., Laurent, O., Tollan, P., Bouvier, A.S., Magna, T., Ulmer, P., France, L., Ellis, B., Bachmann, O., 2022. Degassing from magma reservoir to eruption in silicic systems: the Li elemental and isotopic record from rhyolitic melt inclusions and host quartz in a Yellowstone rhyolite. *Geochim. Cosmochim. Acta* 326, 56–76.
- Paonita, A., 2005. Noble gas solubility in silicate melts: a review of experimentation and theory, and implications regarding magma degassing processes. *Ann. Geophys.* 48, 4–5.
- Pearce, J.A., Norry, M.J., 1979. Petrogenetic implications of Ti, Zr, Y, and Nb variations in volcanic rocks. *Contrib. Mineral. Petrol.* 69, 33–47.
- Phillips, D., Matchan, E.L., 2013. Ultra-high precision ⁴⁰Ar/³⁹Ar ages for fish Canyon Tuff and Alder Creek Rhyolite sanidine: new dating standards required? *Geochim. Cosmochim. Acta* 121, 229–239.
- Plesner, S., Holm, P.M., Wilson, J.R., 2003. ⁴⁰Ar-³⁹Ar geochronology of Santo Antão, Cape Verde Islands. *J. Volcanol. Geotherm. Res.* 120 (1–2), 103–121.

- Popa, R.G., Guillong, M., Bachmann, O., Szymanowski, D., Ellis, B., 2020. U-Th zircon dating reveals a correlation between eruptive styles and repose periods at the Nisyros-Yali volcanic area, Greece. *Chem. Geol.* 555, 119830.
- Preece, K., Barclay, J., Brown, R.J., Chamberlain, K.J., Mark, D.F., 2021. Explosive felsic eruptions on ocean islands: a case study from Ascension Island (South Atlantic). *J. Volcanol. Geotherm. Res.* 416, 107284.
- Putirka, K.D., 2008. Thermometers and barometers for volcanic systems. *Rev. Mineral. Geochem.* 69 (1), 61–120.
- Quidelleur, X., Holt, J.W., Salvany, T., Bouquerel, H., 2010. New K-Ar ages from La Montagne massif, Réunion Island (Indian Ocean), supporting two geomagnetic events in the time period 2.2–2.0 Ma. *Geophys. J. Int.* 182 (2), 699–710.
- Rais, A., Laj, C., Surmont, J., Gillot, P.Y., Guillou, H., 1996. Geomagnetic field intensity between 70 000 and 130 000 years BP from a volcanic sequence on La Réunion, Indian Ocean. *Earth Planet. Sci. Lett.* 140 (1–4), 173–189.
- Rançon, J.P., Rocher, P., 1985. Discovery of recent fumarolic zones in the Cirque de Salazie (Reunion Island, Indian Ocean). *Proc. Acad. Sci. Ser. 2 Mech. Phys. Chem. Sci. Univ. Sci. Earth* 300 (16), 821–826.
- Reddy, S.M., Kelley, S.P., Wheeler, J., 1996. A 40Ar/39Ar laser probe study of micas from the Sesia Zone, Italian Alps: implications for metamorphic and deformation histories. *J. Metamorph. Geol.* 14 (4), 493–508.
- Reiners, P.W., Carlson, R.W., Renne, P.R., Cooper, K.M., Granger, D.E., McLean, N.M., Schoene, B., 2017. Geochronology and Thermochronology. John Wiley & Sons.
- Renne, P.R., Mulcahy, S.R., Cassata, W.S., Morgan, L.E., Kelley, S.P., Hlusko, L.J., Njau, J.K., 2012. Retention of inherited Ar by alkali feldspar xenocrysts in a magma: Kinetic constraints from Ba zoning profiles. *Geochim. Cosmochim. Acta* 93, 129–142.
- Rocher, P., 1988. Volcanic and Structural Context of Recent Hydrothermalism in the Piton Des Neiges Massif (Reunion Island): Detailed Study of the Cirque de Salazie (Doctoral Dissertation, Paris 11).
- Roult, G., Peltier, A., Taisne, B., Staudacher, T., Ferrazzini, V., Di Muro, A., 2012. A new comprehensive classification of the Piton de la Fournaise activity spanning the 1985–2010 period. Search and analysis of short-term precursors from a broad-band seismological station. *J. Volcanol. Geotherm. Res.* 241, 78–104.
- Salvany, T., Lahitte, P., Nativel, P., Gillot, P.Y., 2012. Geomorphic evolution of the Piton des Neiges volcano (Réunion Island, Indian Ocean): competition between volcanic construction and erosion since 1.4 Ma. *Geomorphology* 136 (1), 132–147.
- Sanjuan, B., Traineau, H., Rançon, J.P., Rocher, P., Demange, J., 2000. The geothermal potential of the Reunion Island. In: *Knowledge Assessment and Perspectives*.
- Schaen, A.J., Jicha, B.R., Hodges, K.V., Vermeesch, P., Stelten, M.E., Mercer, C.M., Phillips, D., Rivera, T.A., Jourdan, F., Matchan, E.L., Hemming, S.R., Morgan, L.E., Kelley, S.P., Cassata, W.S., Heizler, M.T., Vasconcelos, P.M., Benowitz, J.A., Koppers, A.A.P., Mark, D.F., Niespolo, E.M., Sprain, C.J., Hames, W.E., Kuiper, K.F., Turrin, B.D., Renne, P.R., Ross, J., Nomade, S., Guillou, H., Webb, L.E., Cohen, B.A., Calvert, A.T., Joyce, N., Ganerod, M., Wijbrans, J., Ishizuka, O., He, H., Ramirez, A., Pfänder, J.A., Lopez-Martínez, M., Qiu, H., Singer, B.S., 2021. Interpreting and reporting 40Ar/39Ar geochronologic data. *Bulletin* 133 (3–4), 461–487.
- Schmitt, A.K., Wetzell, F., Cooper, K.M., Zou, H., Wörner, G., 2010. Magmatic longevity of Laacher See Volcano (Eifel, Germany) indicated by U–Th dating of intrusive carbonatites. *J. Petrol.* 51 (5), 1053–1085.
- Singer, B.S., Wijbrans, J.R., Nelson, S.T., Pringle, M.S., Feeley, T.C., Dungan, M.A., 1998. Inherited argon in a Pleistocene andesite lava: 40Ar/39Ar incremental-heating and laser-fusion analyses of plagioclase. *Geology* 26 (5), 427–430.
- Singer, B.S., Jicha, B.R., Condon, D.J., Macho, A.S., Hoffman, K.A., Dierkhising, J., Brown, M.C., Feinberg, J.M., Kidane, T., 2014. Precise ages of the Réunion event and Huckleberry Ridge excursion: Episodic clustering of geomagnetic instabilities and the dynamics of flow within the outer core. *Earth Planet. Sci. Lett.* 405, 25–38.
- Sliwinski, J.T., Kueter, N., Marxer, F., Ulmer, P., Guillong, M., Bachmann, O., 2018. Controls on lithium concentration and diffusion in zircon. *Chem. Geol.* 501, 1–11.
- Smetana, M., 2011. Petrology, Geochronology (K-Ar) and Elementary and Isotopic Geochemistry (Sr, Nd, Hf, Pb) of Ancient Lava from La Réunion: Implications for the Construction of the Volcanic Edifice. Doctoral dissertation, La Réunion.
- Spera, F.J., Crisp, J.A., 1981. Eruption volume, periodicity, and caldera area: relationships and inferences on development of compositional zonation in silicic magma chambers. *J. Volcanol. Geotherm. Res.* 11 (2–4), 169–187.
- Stelten, M.E., Cooper, K.M., Vazquez, J.A., Calvert, A.T., Glessner, J.J., 2015. Mechanisms and timescales of generating eruptible rhyolitic magmas at Yellowstone caldera from zircon and sanidine geochronology and geochemistry. *J. Petrol.* 56 (8), 1607–1642.
- Sun, Y., Schmitt, A.K., Häger, T., Schneider, M., Pappalardo, L., Russo, M., 2021. Natural blue zircon from Vesuvius. *Mineral. Petrol.* 115 (1), 21–36.
- Thordarson, T., Larsen, G., 2007. Volcanism in Iceland in historical time: Volcano types, eruption styles and eruptive history. *J. Geodyn.* 43 (1), 118–152.
- Townsend, M., Huber, C., Degruyter, W., Bachmann, O., 2019. Magma chamber growth during intercaldera periods: Insights from thermo-mechanical modeling with applications to Laguna del Maule, Campi Flegrei, Santorini, and Aso. *Geochim. Geophys. Geosyst.* 20 (3), 1574–1591.
- Trail, D., Watson, E.B., Tailby, N.D., 2012. Ce and Eu anomalies in zircon as proxies for the oxidation state of magmas. *Geochim. Cosmochim. Acta* 97, 70–87.
- Turner, G., Miller, J.A., Grasty, R.L., 1966. The thermal history of the Bruderheim meteorite. *Earth Planet. Sci. Lett.* 1 (4), 155–157.
- Upton, B.G.J., 1982. Oceanic islands. In: *The Ocean Basins and Margins*. Springer, Boston, MA, pp. 585–648.
- Upton, B.G.J., Wadsworth, W.J., 1966. The basalts of Reunion Island, Indian Ocean. *Bull. Volcanol.* 29 (1), 7–23.
- Upton, B.G.J., Wadsworth, W.J., 1967. A complex basalt-mugearite sill in Piton des Neiges volcano, Reunion. *American Mineralogist*. *J. Earth Planet. Mater.* 52 (9–10), 1475–1492.
- Valer, M., Bachèlery, P., Schiano, P., 2017. The petrogenesis of plagioclase-ultraphyric basalts from La Réunion Island. *J. Petrol.* 58 (4), 675–698.
- Van den Bogaard, P., Schirnick, C., 1995. 40Ar/39Ar laser probe ages of Bishop Tuff quartz phenocrysts substantiate long-lived silicic magma chamber at Long Valley, United States. *Geology* 23 (8), 759–762.
- Van Zalinge, M.E., Mark, D.F., Sparks, R.S.J., Tremblay, M.M., Keller, C.B., Cooper, F.J., Rust, A., 2022. Timescales for pluton growth, magma-chamber formation and super-eruptions. *Nature* 608 (7921), 87–92.
- Wartho, J.A., Kelley, S.P., Brooker, R.A., Carroll, M.R., Villa, I.M., Lee, M.R., 1999. Direct measurement of Ar diffusion profiles in a gem-quality Madagascar K-feldspar using the ultra-violet laser ablation microprobe (UVALMP). *Earth Planet. Sci. Lett.* 170 (1–2), 141–153.
- Wijbrans, J.R., McDougall, I., 1988. Metamorphic evolution of the attic Cycladic Metamorphic Belt on Naxos (Cyclades, Greece) utilizing 40Ar/39Ar age spectrum measurements. *J. Metamorph. Geol.* 6 (5), 571–594.